Detecting Cosmological Stasis with Future Gravitational Wave Observatories

Gabriela Barenboim[1,2] and Anne-Katherine Burns[3,4]

[1]*Instituto de Física Corpuscular, CSIC-Universitat de València, Paterna 46980, Spain*

[2]*Departament de Física Teòrica, Universitat de València, Burjassot 46100, Spain*

[3]*Departament de Física Quàntica i Astrofísica (FQA),*
Universitat de Barcelona (UB), c. Martí i Franquès, 1, 08028 Barcelona, Spain

[4]*Institut de Ciències del Cosmos (ICCUB), Universitat de Barcelona (UB),*
*c. Martí i Franquès, 1, 08028 Barcelona, Spain**

arXiv:2607.18449v1 [hep-ph] 20 Jul 2026

Abstract

We map the observational predictions of cosmological stasis in the inflationary gravitational wave background (IGWB) onto the sensitivity bands of current and planned gravitational wave detectors. Using the closed-form piecewise spectral template derived in the companion paper [1], we generate detectability maps for four stasis scenarios — canonical ($0 \leq w_s < 1/3$), dynamical scalar ($1/3 < w_s < 1$), vacuum-energy/matter ($-1/3 < w_s < 0$), and vacuum-energy/radiation ($-1/3 < w_s < 1/3$) — across the frequency bands probed by NANOGrav, SKA, LISA, DECIGO, BBO, the Einstein Telescope, and Cosmic Explorer. For scenarios in which the spectrum is suppressed, $w_s < 1/3$, the stasis feature is detectable by BBO in the region of $(w_s, \Delta N)$ parameter space in which $w_s \gtrsim 0.2$ for tensor-to-scalar ratios close to the Planck upper limit, r = 0.036, while to be detectable by DECIGO requires $w_s \gtrsim 0.3$. For scenarios in which the spectrum is enhanced, $w_s > 1/3$, the stasis feature is detectable by BBO across the entire $(w_s, \Delta N)$ parameter space for tensor-to-scalar ratios of $O(0.01)$. For large values of w_s close to the kination limit, the feature is detectable for r as small as 10^{-9}. We characterize the Standard-Model (SM) g_* fine structure of the IGWB, showing that SM phase transitions introduce spectral steps of $\approx 20\%$ (electroweak, at $\sim 2.6 \times 10^{-6}$ Hz) and $\approx 53\%$ (QCD, at $\sim 3.6 \times 10^{-9}$ Hz). For stasis scenarios with end-of-stasis temperatures below the QCD scale these steps fall inside the stasis band and constitute additional spectral features that complement the primary signature. Finally, we model the finite-width end-of-stasis transition phenomenologically, demonstrating that the spectral break at $f_{\rm end}$ is smoothed over a log-frequency window $\Delta N_{\rm trans} \times 3(1+w_s)/4$, and that the consistency relation $\mathcal{C}^2 = \mathcal{C}^2(\alpha)$ remains testable provided $\Delta N_{\rm stasis} \gg \Delta N_{\rm trans}$, a condition easily satisfied for all scenarios of phenomenological interest.

CONTENTS

I. Introduction 4

II. Summary of the stasis GW template 6

A. The piecewise spectral template 6

B. IGWB normalization 7

C. The consistency relation 7

* gabriela.barenboim@uv.es; annekatherineburns@icc.ub.edu

III. The g_* fine structure 8
A. Standard-Model phase transitions and spectral steps 8
B. Correction to $f_{\rm end}$ near the SM transitions 10
C. Spectral steps within the stasis band 10
D. Practical impact on parameter estimation 10

IV. Detectability 11
A. Setup 11
B. Detectability maps 13
C. Microphysical Realizations of Stasis 17
1. Canonical stasis ($0 \leq w_s < 1/3$) 17
2. Dynamical scalar stasis ($1/3 < w_s < 1$) 18
D. Consistency with the $\Delta N_{\rm eff}$ bound 20
E. Which microphysical realizations land where? 23

V. End-of-stasis transition: a phenomenological treatment 25
A. The transition width $\Delta N_{\rm trans}$ 26
B. How the transition smooths the spectrum 26
Deep sub-horizon modes are unaffected 27
Sharp transitions and Bogoliubov oscillations 28
C. Consequences for future observation 28

VI. Discussion and outlook 29

Acknowledgments 31

References 31

A. Vacuum-energy/matter stasis ($-1/3 < w_s < 0$) 33

B. Vacuum-energy/radiation stasis ($-1/3 < w_s < 1/3$) 33

C. Additional plots: r = 0.036 34

I. INTRODUCTION

Cosmological stasis is a dynamical fixed point of the early universe in which the energy fractions Ω_i of multiple components remain exactly constant over an extended epoch, even as the universe expands and dilutes [2]. Unlike the standard cosmological picture in which radiation, matter, and vacuum energy each come to dominate in succession with only transient periods of comparable contributions, stasis is a non-trivial attractor in which an ongoing energy source continuously compensates the dilution from Hubble expansion, locking the total equation of state at a constant value $w_s = \sum_i w_i \Omega_i$. Stasis has been realized in a growing variety of microphysical settings: towers of decaying species [2], populations of primordial black holes evaporating via Hawking radiation [3, 4], dynamical scalars [5], thermal annihilation [6, 7], field-dependent decay [8], and purely gravitational interactions [9]. The recent argument of [10] that stasis is a generic dynamical outcome of multi-component cosmologies further motivates a systematic observational study.

The inflationary gravitational wave background (IGWB) provides a direct observational window into the expansion history of the universe before BBN at energy scales inaccessible to any other probe [11–13]. Because each mode of the IGWB carries an imprint of the equation of state at its horizon re-entry, a stasis epoch of duration ΔN e-folds leaves a characteristic feature in $h^2\Omega_{\rm GW}(f)$ across the frequency band $[f_{\rm end}, f_{\rm beg}]$ corresponding to modes that crossed the horizon during stasis. The attractor enforces $w_s = \text{const}$, which makes the tensor mode equation an exact Bessel equation and allows the entire spectral distortion to be written in closed form.

In the companion paper [1] we derived this closed-form template, established the consistency relation $\mathcal{C}^2 = \mathcal{C}^2(\alpha)$ between the spectral slope and the amplitude step, showed that these two quantities are independently measurable and their combination is falsifiable without knowing w_s in advance, and validated the framework against the numerical PBH-stasis calculation of [3]. The present paper takes the observational step: we ask which current and planned detectors can actually detect the stasis signature, what the minimum tensor-to-scalar ratio r is for a stasis epoch to be detectable in each detector, and what additional spectral features distinguish the stasis scenario from competing models.

The main results of this paper are as follows.

- **Detectability of Suppression Scenarios:** For scenarios in which the spectrum is sup-

pressed, $w_s < 1/3$, BBO can detect the stasis feature for values of $w_s \gtrsim 0.2$ for values of r close to the Planck upper limit, 0.036; while DECIGO requires $w_s \gtrsim 0.3$; LISA, ET, and CE are competitive only for r well above current upper limits. The primary observational target for stasis detection when $w_s < 1/3$ in the IGWB is therefore BBO, in the decade 0.01–1 Hz.

- **Detectability of Enhancement Scenarios:** For scenarios in which the spectrum is enhanced, $w_s > 1/3$, both BBO and DECIGO can detect the stasis feature across the entire $(w_s, \Delta N)$ parameter space for values of r of $O(0.01)$. For values of w_s close to the kination limit, BBO can detect the stasis features for r values as small as $\sim 10^{-9}$. For stasis configurations with the longest durations thereby spanning the widest frequency bands, LISA and CE are competitive when r is of $O(0.01)$ for $w_s \gtrsim 0.55$ and ET is competitive when r is of $O(0.01)$ for $w_s \gtrsim 0.65$.

- **g_* fine structure:** The Standard-Model phase transitions at the electroweak ($T_{\rm EW} \sim 100\,{\rm GeV}$) and QCD ($T_{\rm QCD} \sim 150\,{\rm MeV}$) scales suppress the spectrum at frequencies above each transition by approximately 20% (electroweak) and 53% (QCD) relative to the spectrum below at the corresponding frequencies $f_{\rm EW} \approx 2.6 \times 10^{-6}\,{\rm Hz}$ and $f_{\rm QCD} \approx 3.6 \times 10^{-9}\,{\rm Hz}$. For stasis scenarios with $T_{\rm end} \lesssim T_{\rm QCD}$, both steps fall inside the stasis band and are superimposed on the power-law tilt.

- **Smooth transition:** The finite-width transition out of stasis smooths the spectral break at $f_{\rm end}$ over a log-frequency window $\Delta \ln f = 3(1 + w_s)/4 \cdot \Delta N_{\rm trans}$, leaving a measurable shoulder whose width encodes the transition microphysics. The consistency relation remains intact provided $\Delta N_{\rm stasis} \gg \Delta N_{\rm trans}$.

This paper is organized as follows. Section II summarizes the key results from [1] that are used in the rest of the paper. Section III derives the g_* fine structure of the IGWB and its interplay with the stasis template. Section IV presents the detectability maps for the two stasis scenarios across three representative frequency bands, with detectability maps for two additional scenarios appearing in the appendix. Section V develops the phenomenological treatment of the smooth end-of-stasis transition. We conclude in Sec. VI.

II. SUMMARY OF THE STASIS GW TEMPLATE

We summarize the results of [1] that enter the detectability analysis. The full derivations are given there; here we collect only the operational formulae.

A. The piecewise spectral template

Because the stasis attractor enforces a constant equation of state w_s, the expansion during stasis is an exact power law in conformal time and the tensor mode equation reduces to a Bessel equation with index

$$\nu(w_s) = \frac{3(1-w_s)}{2(1+3w_s)}. \tag{1}$$

The sub-horizon WKB amplitude acquires the Bessel coefficient

$$\mathcal{C}^2(\nu) = \left[\frac{2^{\nu+1/2}\,\Gamma(\nu+1)}{\sqrt{\pi}\,\beta^\beta}\right]^2, \qquad \beta \equiv \frac{2}{1+3w_s}, \tag{2}$$

which satisfies $\mathcal{C}^2(1/2) = 1$ (radiation domination) and $\mathcal{C}^2(3/2) = 9/16$ (matter domination). The spectral distortion relative to the radiation-dominated baseline is

$$\alpha(w_s) = \frac{2(3w_s-1)}{1+3w_s}, \tag{3}$$

which is negative, corresponding to a suppression or "notch" for canonical stasis $w_s < 1/3$ and positive, corresponding to an enhancement for $w_s > 1/3$.

The IGWB spectrum is piecewise:

$$h^2\Omega_{\rm GW}(f) = h^2\Omega_{\rm GW}^{(\rm RD)}(f) \times \begin{cases} 1 & f < f_{\rm end}, \\ \mathcal{C}^2(\nu)\left(f/f_{\rm end}\right)^{\alpha(w_s)} & f_{\rm end} < f < f_{\rm beg}, \\ \left(f_{\rm beg}/f_{\rm end}\right)^{\alpha(w_s)} & f > f_{\rm beg}, \end{cases} \tag{4}$$

where $h^2\Omega_{\rm GW}^{(\rm RD)}$ is the standard flat IGWB (see Sec. II B below), and the lower break frequency is

$$f_{\rm end} = \frac{T_0\,T_{\rm end}}{2\sqrt{90}\,\bar{M}_{\rm Pl}}\sqrt{g_*(T_{\rm end})}\left(\frac{g_{*s,0}}{g_{*s}(T_{\rm end})}\right)^{1/3}\frac{1}{\hbar} \;\approx\; 2.65\times10^{-8}\,{\rm Hz}\left(\frac{T_{\rm end}}{1\,{\rm GeV}}\right)\left(\frac{g_*(T_{\rm end})}{106.75}\right)^{1/6}, \tag{5}$$

where T_0 is the CMB temperature today, $T_{\rm end}$ is the final temperature of the stasis epoch, $\bar{M}_{\rm Pl}$ is the reduced Planck mass, and the approximate form assumes $g_* \approx g_{*s}$. The upper break frequency is $f_{\rm beg} = f_{\rm end}\,\exp\!\big[(1+3w_s)\Delta N/2\big]$, and the stasis duration is $\Delta N = \ln(f_{\rm beg}/f_{\rm end})\cdot 2/(1+3w_s)$. Table I collects $\mathcal{C}^2$ for several representative equations of state.

Era	w_s	α	ν	$\mathcal{C}^2$
Matter domination (MD)	0	-2	3/2	0.5625
Stasis ($w_s = 1/6$)	1/6	$-2/3$	5/6	0.8304
Radiation domination (RD)	1/3	0	1/2	1.0000
Kination	1	$+1$	0	$4/\pi$

TABLE I: Spectral tilt α, Bessel index ν, and amplitude coefficient $\mathcal{C}^2(\nu)$ for several reference equations of state. The value $\mathcal{C}^2 = 1$ is recovered for radiation domination, and $\mathcal{C}^2 < 1$ for all $w_s < 1/3$ (canonical stasis, matter domination).

B. IGWB normalization

For a nearly scale-invariant primordial tensor spectrum with tensor-to-scalar ratio r evaluated at the pivot scale $k_* = 0.05\,\mathrm{Mpc}^{-1}$, the flat IGWB amplitude in the radiation-dominated limit is

$$h^2\Omega_{\mathrm{GW}}^{(\mathrm{RD})} \simeq \frac{3}{128}\, h^2\Omega_{r,0}\, r\, A_s \left(\frac{g_*}{g_{*0}}\right)^{-1/3} \approx 6.8\times 10^{-18} \left(\frac{r}{0.01}\right)\left(\frac{g_*}{106.75}\right)^{-1/3}, \tag{6}$$

where $h^2\Omega_{r,0} \approx 4.17\times 10^{-5}$, $A_s \approx 2.1\times 10^{-9}$ [14], and $g_{*0} \equiv g_*(T_{\mathrm{beg}})$ is evaluated at the horizon-entry temperature; the approximate numerical form normalizes to the SM value $g_* = 106.75$ (valid for $T_{\mathrm{beg}} \gg T_{\mathrm{EW}}$). The current upper limit $r < 0.036$ (Planck + BICEP/Keck [15]) sets $h^2\Omega_{\mathrm{GW}}^{(\mathrm{RD})} \lesssim 2.4\times 10^{-17}$, well below the sensitivities of LISA and ET but within reach of BBO and DECIGO (see Sec. IV).

C. The consistency relation

As derived in [1], the spectral tilt α and the amplitude step $\mathcal{C}^2$ are both determined by a single underlying quantity w_s, and their relationship traces a one-dimensional curve $\mathcal{C}^2 = \mathcal{C}^2(\alpha)$ in the $(\alpha, \mathcal{C}^2)$ plane, as shown in the following equation.

$$\mathcal{C}^2 = \mathcal{C}^2(\alpha) \equiv \left[\frac{2^{\nu(\alpha)+1/2}\,\Gamma(\nu(\alpha)+1)}{\sqrt{\pi}\,\beta(\alpha)^{\beta(\alpha)}}\right]^2, \quad \nu = \frac{1-\alpha}{2}, \quad \beta = \frac{2-\alpha}{2}. \tag{7}$$

This curve is a universal Bessel-function relation satisfied by every constant-w era, regardless of the underlying microphysical mechanism. Because α can be measured independently from the slope of the stasis band and $\mathcal{C}^2$ can be measured from the amplitude step at $f_{\rm end}$, the curve provides a falsifiable internal consistency test: a data point that lands off the curve indicates either a time-varying equation of state, a multi-component fluid, or systematic uncertainties in the detector model.

III. THE g_* FINE STRUCTURE

The IGWB is not perfectly flat even in the absence of stasis. As modes of different frequency crossed the cosmological horizon at different temperatures, they experienced different effective numbers of relativistic degrees of freedom $g_*(T)$. The resulting g_*-induced spectral modulation is a known prediction of Standard Model thermodynamics and constitutes a background "fine structure" on top of which the stasis imprint sits. In this section we characterize this fine structure, identify which frequency bands are affected, and discuss its interplay with the stasis template.

A. Standard-Model phase transitions and spectral steps

The energy density of the IGWB for modes entering the horizon at temperature T scales as [13, 16]

$$h^2\Omega_{\rm GW}^{(\rm RD)}(f) \propto g_*(T(f))^{-1/3}, \tag{8}$$

where $T(f)$ is the temperature at horizon entry for mode f. The proportionality constant is absorbed into the normalization of eq. (6), which is evaluated at $g_* = 106.75$. As $g_*(T)$ decreases through a phase transition, modes that entered the horizon just below the transition temperature see a smaller g_* and therefore have a *larger* $h^2\Omega_{\rm GW}$: the spectrum steps up when moving from high to low frequency through a transition. The step amplitude is set by the ratio of g_* values on each side and is independent of normalization convention.

The Standard Model predicts two relevant transitions in the cosmological frequency range:

1. **Electroweak crossover** ($T_{\rm EW} \approx 100\,\mathrm{GeV}$): g_* drops from 106.75 (above) to $\approx$ 61.75

(below) over time, producing a spectral step of

$$\frac{h^2\Omega_{\rm GW}(f < f_{\rm EW})}{h^2\Omega_{\rm GW}(f > f_{\rm EW})} = \left(\frac{106.75}{61.75}\right)^{1/3} \approx 1.20, \tag{9}$$

at the frequency

$$f_{\rm EW} \approx 2.65 \times 10^{-8}\,{\rm Hz} \times (T_{\rm EW}/{\rm GeV}) \approx 2.6 \times 10^{-6}\,{\rm Hz}. \tag{10}$$

2. **QCD crossover** ($T_{\rm QCD} \approx 150\,{\rm MeV}$): g_* drops from ≈ 61.75 (above) to ≈ 17.25 (below, after quark–hadron transition and pion decoupling), producing a step of

$$\frac{h^2\Omega_{\rm GW}(f < f_{\rm QCD})}{h^2\Omega_{\rm GW}(f > f_{\rm QCD})} = \left(\frac{61.75}{17.25}\right)^{1/3} \approx 1.53, \tag{11}$$

at

$$f_{\rm QCD} \approx 2.65 \times 10^{-8}\ {\rm Hz} \times 0.150 \times (g_*/106.75)^{1/6}\ \approx 3.6 \times 10^{-9}\,{\rm Hz} \tag{12}$$

for $g_* = 61.75$. These steps are fixed, known features of the IGWB that do not depend on the stasis parameters. In the context of a stasis search, they can serve as calibration points or, when they fall inside the stasis band, as complicating features that must be modeled.

The two transitions above are not equally sharp. The QCD crossover is a genuinely rapid transition on cosmological time scales: the quark-hadron transition and pion decoupling occur over a narrow temperature window, $\Delta T/T \sim \mathcal{O}(1)$, so modeling it as an instantaneous step in $g_*(T)$, as in eq. (11), is an accurate approximation [17]. The electroweak transition is different in character. As the plasma cools through $T \sim 100$–$200\,{\rm GeV}$, the top quark, Higgs boson, $W^\pm$, Z, and bottom quark become non-relativistic in succession rather than simultaneously, with their masses spanning $m_b \approx 4.2\,{\rm GeV}$ to $m_t \approx 173\,{\rm GeV}$, roughly two decades in temperature. The corresponding change in $g_*(T)$ near $T_{\rm EW}$ is therefore not a single sharp step but a smooth roll-off spread over the corresponding range in horizon-entry frequency, $f \sim 10^{-7}$–$10^{-5}\,{\rm Hz}$ by eq. (5). The instantaneous-step treatment of eq. (9) should accordingly be understood as a schematic approximation to this smoother feature: it correctly captures the total amplitude change and the characteristic frequency scale, but not the detailed shape of the transition. In the figures we replace the step in eq. (9) with the smoothed profile obtained by integrating eq. (8) against the full SM $g_*(T)$ table [17] while the QCD step remains sharp. This refinement does not affect the order-of-magnitude conclusions of this section, but it does change the detailed shape of the high-frequency feature, which is now visible as a broad shoulder rather than a step in all figures in which the EW frequency range is visible.

B. Correction to $f_{\rm end}$ near the SM transitions

The break-frequency formula of eq. (5) includes a factor $g_*(T_{\rm end})^{1/6}$ that depends on the SM degrees of freedom at the end of stasis. For $T_{\rm end}$ well above the EW scale, $g_* = 106.75$ and the approximate formula is exact. Near or below the SM transitions, however, the correct value of $g_*(T_{\rm end})$ deviates significantly:

- $T_{\rm end} \approx 150\,\text{MeV}$ (QCD scale): $g_* \approx 61.75$, giving an 8.7% downward correction to $f_{\rm end}$ relative to the naive $g_* = 106.75$ estimate.
- $T_{\rm end} \approx 55\,\text{MeV}$: $g_* \approx 10.75$, giving a 32% downward correction. The naive $g_* = 106.75$ formula overestimates $f_{\rm end}$ by nearly 50%.

When performing a stasis template fit to data, the correct $g_*(T_{\rm end})$ must therefore be inserted into eq. (5), using tabulated SM $g_*(T)$ values [17]. Equivalently, $T_{\rm end}$ can be treated as a free parameter whose relationship to $f_{\rm end}$ is computed from the full SM thermodynamic history.

C. Spectral steps within the stasis band

The most striking effect of g_* fine structure occurs when a SM transition temperature $T_{\rm trans}$ falls within the range $[T_{\rm end}, T_{\rm beg}]$ probed by the stasis band. In that case, the transition frequency $f_{\rm trans}$ lies inside $[f_{\rm end}, f_{\rm beg}]$, and the otherwise smooth power-law tilt α in the stasis band is interrupted by a g_*-induced step. In Section IV A, we discuss this impact in detail for each of the configurations we consider here. These steps can be seen in Fig. 2 (see §IV A).

D. Practical impact on parameter estimation

The g_* fine structure modifies the parameter-estimation problem for frequency bands where internal g_* steps are present in which stasis occurs in two important ways.

First, the internal steps at $f_{\rm QCD}$ and $f_{\rm EW}$ break the simple power law in the stasis band. A naive fit of α from the slope across the full stasis band would be biased by the presence of the steps; instead, the slope should be fit over segments between the steps ($f_{\rm end} < f < f_{\rm QCD}$, $f_{\rm QCD} < f < f_{\rm EW}$, and $f_{\rm EW} < f < f_{\rm beg}$), each of which still has slope $\alpha(w_s)$, and the fit should explicitly include the step amplitudes as predicted by the SM thermal history.

Second, the two steps which occur at fixed, theoretically known frequencies serve as internal calibration points. The same g_* history that produces the steps also sets the overall IGWB normalization via eq. (8), providing a self-consistency check between the step amplitudes and the continuum shape. A mismatch between the observed step amplitude and the SM prediction would signal new physics, e.g., additional light degrees of freedom active near the relevant transition temperature.

As discussed in Section IV A, for the frequency bands in which stasis occurs where no internal g_* steps are present, the stasis template in its idealized form (4) is directly applicable with only the overall normalization correction from eq. (8). The g_* correction to $f_{\rm end}$ (Sec. III B) should nonetheless be applied when inverting an observed $f_{\rm end}$ to a physical temperature $T_{\rm end}$.

Note. The g_* fine structure of the IGWB is a predicted feature of Standard Model thermodynamics. In the context of a stasis search, the steps at $f_{\rm QCD}$ and $f_{\rm EW}$ are *not* free parameters: their frequencies and amplitudes are fixed by the SM. A detection of stasis in a frequency band in which internal g_* steps are present should therefore simultaneously reproduce the known g_* steps at the correct frequencies, providing a non-trivial cross-check of both the stasis hypothesis and Standard Model thermodynamics.

IV. DETECTABILITY

A. Setup

We overlay the stasis GW template of eq. (4) on the power-law integrated sensitivity (PLS) curves [18] of the following instruments: NANOGrav [19], EPTA [20], SKA [21], LISA [22], DECIGO [23], BBO [24], Einstein Telescope (ET-D) [25], and Cosmic Explorer (CE) [26]. We also show the NANOGrav 15-year posterior [27] as a reference blue band.

All spectra are shown relative to the IGWB reference baseline at $r = 0.01$ (grey dashed line), which gives $h^2\Omega_{\rm GW}^{\rm (RD)} \approx 6.8 \times 10^{-18}$ at high frequency. For each scenario we choose three representative frequency-band configurations:

- **Band I:** $f_{\rm end} = 10^{-4}\,{\rm Hz}$, $f_{\rm beg} = 10^{-1}\,{\rm Hz}$, squarely in the LISA band. Corresponds to $T_{\rm end} \approx 3.8\,{\rm TeV}$, well above the electroweak scale. Here, the stasis band has $g_* = 106.75$ throughout. No internal g_* steps; only the overall normalization correction (8) applies.

- **Band II:** $f_{\rm end} = 10^{-9}\,{\rm Hz}$, $f_{\rm beg} = 10^{-2}\,{\rm Hz}$, spanning the PTA-to-LISA range. Corresponds to $T_{\rm end} \approx 55\,{\rm MeV}$, below the QCD crossover. Here, $f_{\rm QCD} \approx 3.6 \times 10^{-9}\,{\rm Hz}$ and $f_{\rm EW} \approx 2.6 \times 10^{-6}\,{\rm Hz}$ both fall inside $[f_{\rm end}, f_{\rm beg}] = [10^{-9}, 10^{-2}]\,{\rm Hz}$. The stasis band therefore contains *two additional spectral steps* of $\approx 53\%$ (QCD) and $\approx 20\%$ (EW) superimposed on the power-law tilt $\alpha(w_s)$. These steps are at known, fixed frequencies and are distinct from the stasis breaks at $f_{\rm end}$ and $f_{\rm beg}$. Note, however, that $f_{\rm QCD} \approx 3.6\, f_{\rm end}$ for this configuration, so the QCD step sits close to the lower break; a joint template fit including both the stasis break at $f_{\rm end}$ and the g_*-induced step at $f_{\rm QCD}$ is necessary to avoid bias.

- **Band III:** $f_{\rm end} = 10^{-2}\,{\rm Hz}$, $f_{\rm beg} = 10^{3}\,{\rm Hz}$, spanning DECIGO/BBO to ET/CE. Corresponds to $T_{\rm end} \approx 380\,{\rm TeV}$. As in Band I, both transition frequencies lie below $f_{\rm end}$. No internal g_* steps.

These three bands have been intentionally chosen to probe distinct thermal scales rather than to span equal frequency ranges. Table II summarizes these configurations and the corresponding thermal scales.

Band	$f_{\rm end}$	$f_{\rm beg}$	$T_{\rm end}$	Primary detector(s)
I	$10^{-4}\,{\rm Hz}$	$10^{-1}\,{\rm Hz}$	$\sim 3.8\,{\rm TeV}$	LISA
II	$10^{-9}\,{\rm Hz}$	$10^{-2}\,{\rm Hz}$	$\sim 55\,{\rm MeV}$	NANOGrav, SKA, LISA
III	$10^{-2}\,{\rm Hz}$	$10^{3}\,{\rm Hz}$	$\sim 380\,{\rm TeV}$	BBO, DECIGO, ET, CE

TABLE II: Frequency-band configurations used in the detectability plots. The break-frequency-to-temperature mapping uses eq. (5) with g_* fine structure corrections included. The g_* correction for Band II is discussed in Sec. III.

Figures 1, 2, and 3 show the spectral shape for a range of w_s values across all three bands, illustrating how the spectral tilt and amplitude step evolve across the parameter space. It is important to note that for some stasis epochs, the frequency band during which stasis occurs might be such that an enhancement or suppression, and therefore the spectral distortion, α, is measurable by a detector but the amplitude step, $\mathcal{C}^2$ is not. While a measured slope, α is a hint that a stasis epoch occurred, the consistency relation $\mathcal{C}^2 = \mathcal{C}^2(\alpha)$ of Eq. 7 is what makes the

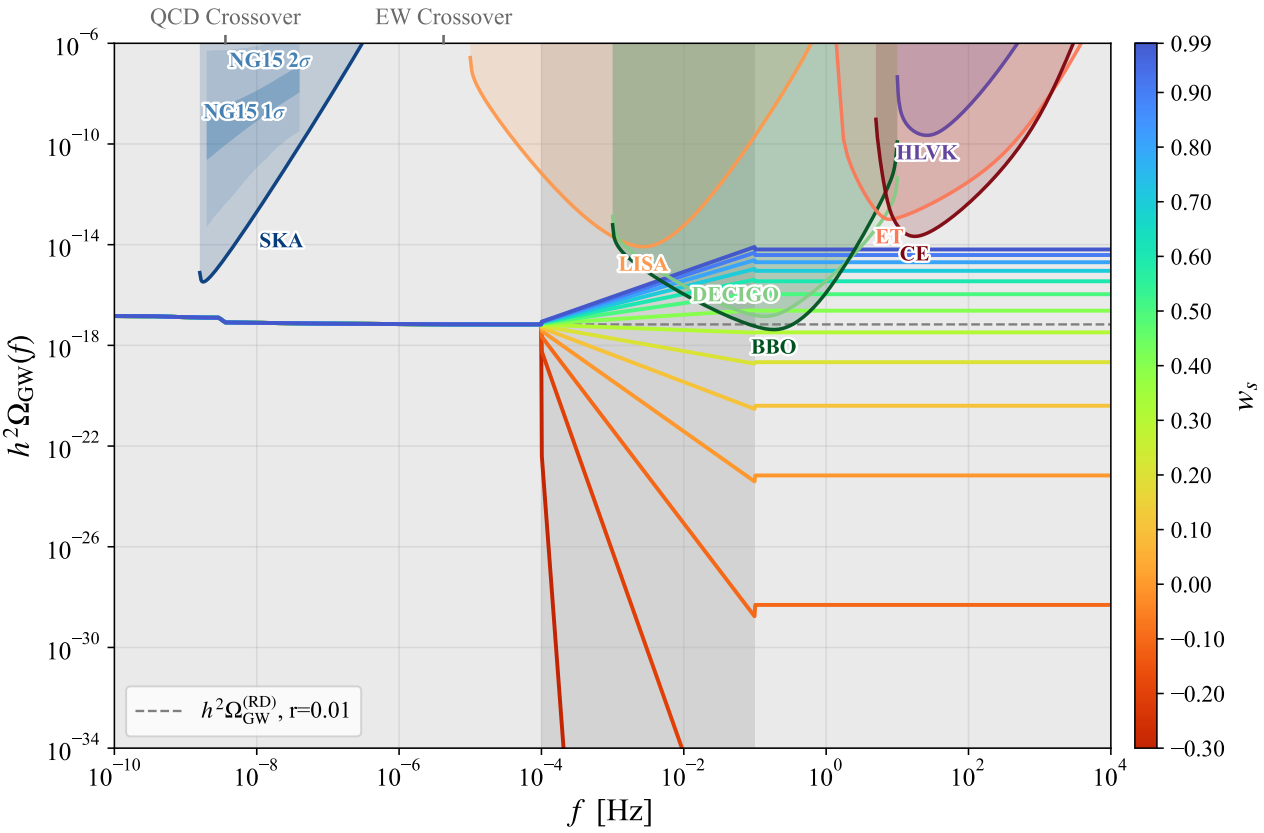


FIG. 1: Stasis-modified IGWB for several equations of state $w_s \in [-1/3, 1]$ in Band I ($f_{\rm end} = 10^{-4}$ Hz, $f_{\rm beg} = 10^{-1}$ Hz). Shaded regions: PLS curves [18] with $T_{obs} = 4$ years and $\rho_{thr} = 1$. Grey dashed: RD baseline at $r = 0.01$. The g_* fine structure, discussed in Section III is incorporated in all spectra.

test specific to stasis, and that requires both quantities to be independently measurable. In the Band III case as shown in Fig. 3, for $w_s > 0.3$, the suppression or enhancement is measurable, but the amplitude step is not meaning that if stasis were to have occurred during this time, our projected future detector landscape would be unable to verify it through the consistency relation.

B. Detectability maps

In Sec. IV A we fix both the tensor-to-scalar ratio, r, and the stasis duration, ΔN and display the resulting shape. Here, we show for each point on the (w_s, r) plane the length of time a stasis epoch must last for its imprint to be resolvable at all. To do this, we require that the flat

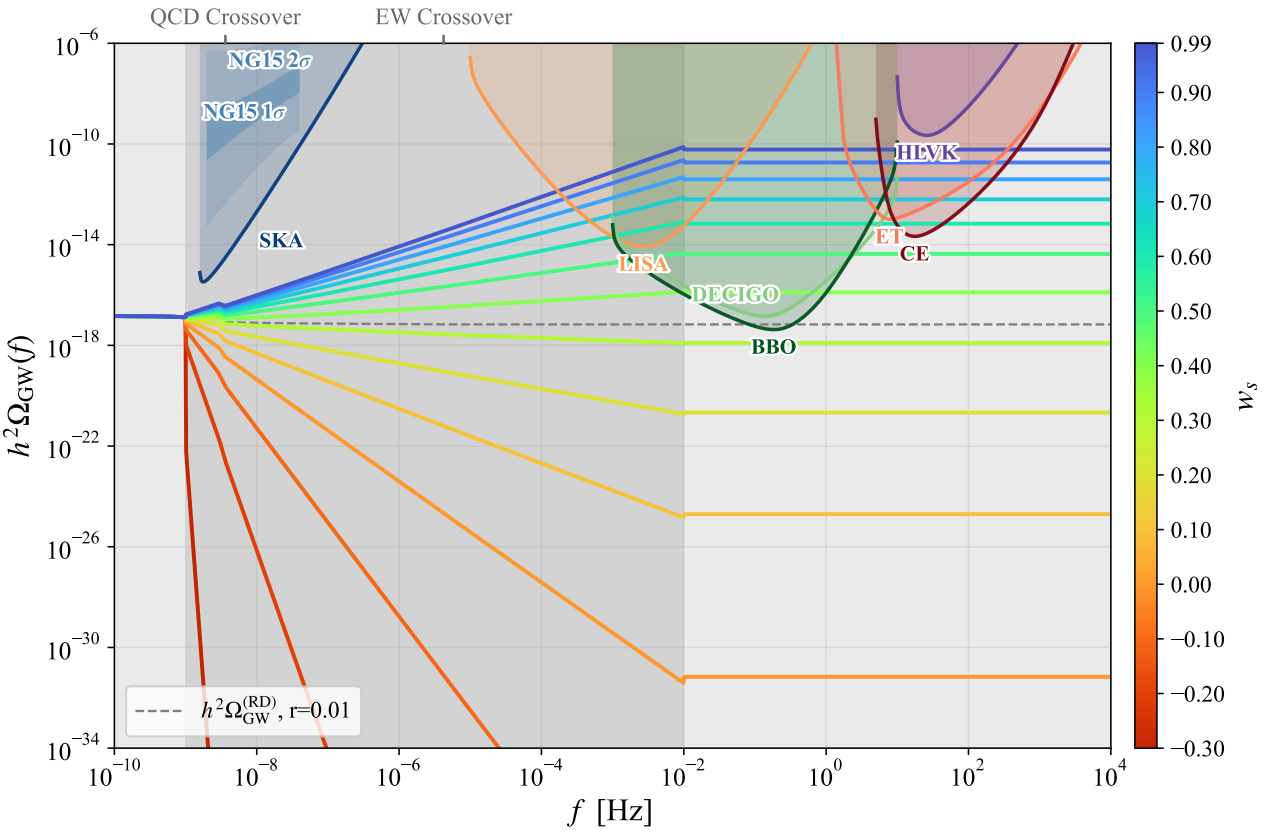


FIG. 2: Same as Fig. 1 for Band II ($f_{\rm end} = 10^{-9}\,$Hz, $f_{\rm beg} = 10^{-2}\,$Hz). The g_* fine structure of Sec. III adds spectral steps at $f_{\rm QCD} \approx 3.6 \times 10^{-9}\,$Hz and $f_{\rm EW} \approx 2.6 \times 10^{-6}\,$Hz, which fall inside the stasis band for this configuration.

region below $f_{\rm end}$, which fixes $\mathcal{C}^2$, or the elevated region above $f_{\rm beg}$, which fixes $\mathcal{C}^2(f_{\rm beg}/f_{\rm end})^\alpha$ along with some part of the tilted stasis band must cross the PLS curve of the same instrument. Requiring only that the tilted stasis band $[f_{\rm end}, f_{\rm beg}]$ rise above the PLS curve is sufficient to measure the slope α and hence w_s, but as emphasized in Sec. IV A a measured slope alone is a hint rather than a test: the consistency relation $\mathcal{C}^2 = \mathcal{C}^2(\alpha)$ of eq. (7) is what makes the signature specific to stasis, and it requires the amplitude step at $f_{\rm end}$ to be measurable independently.

At fixed w_s and $f_{\rm end}$, $r_{\rm min}$ decreases monotonically with ΔN and then saturates, so it may be inverted to give the shortest stasis epoch that a given tensor amplitude renders detectable,

$$\Delta N_{\rm min}(w_s, r) \;\equiv\; \min\big\{\Delta N \,:\, r_{\rm min}(w_s, \Delta N) \le r\big\}, \tag{13}$$

which is the quantity mapped in Fig. 4. Each map fixes $f_{\rm end}$ at one of the three band

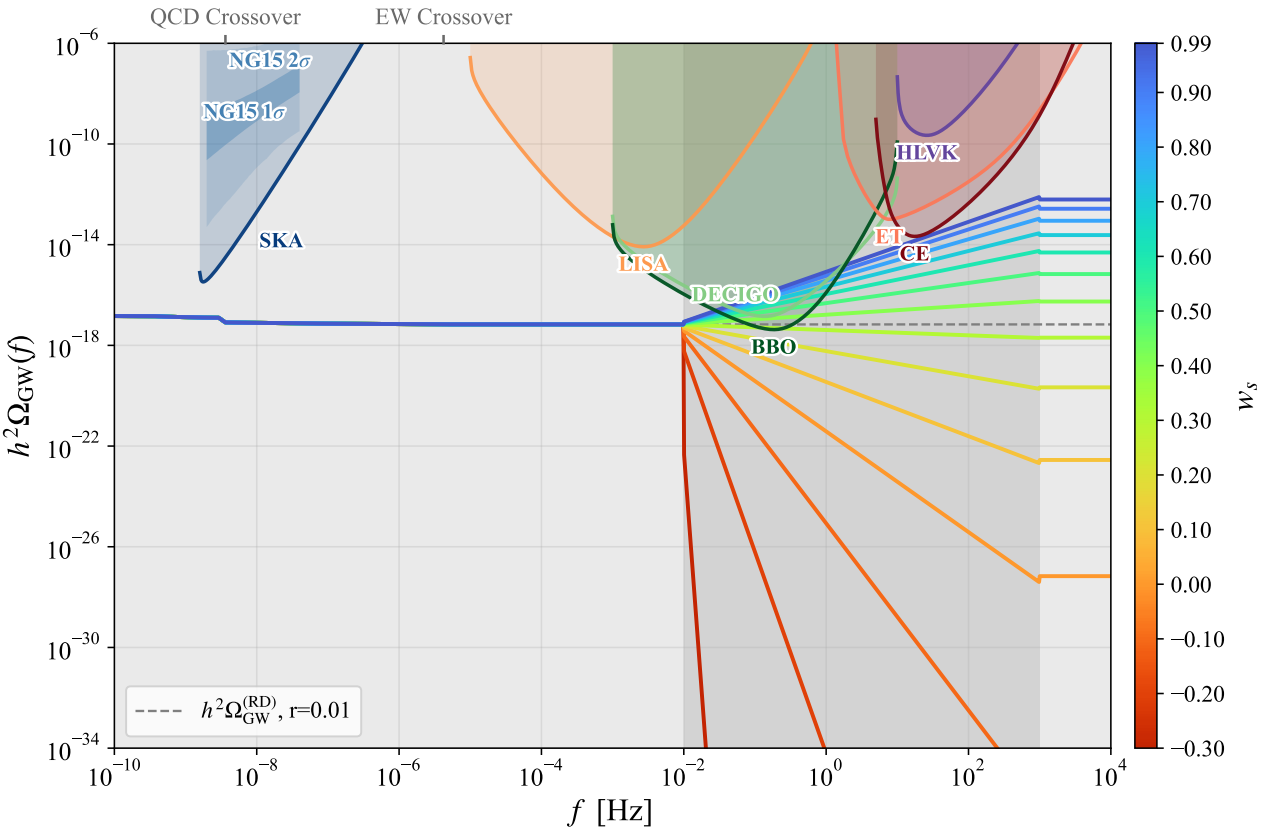
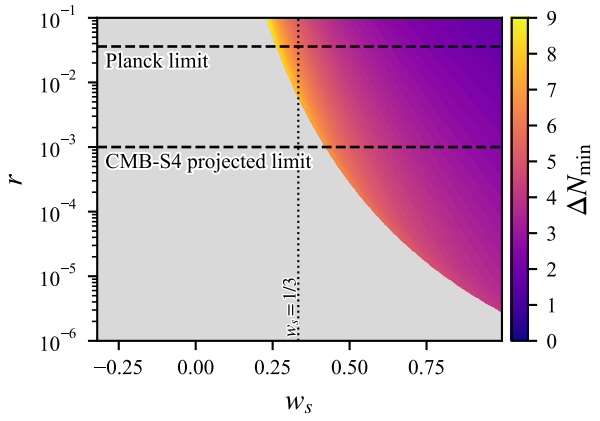


FIG. 3: Same as Fig. 1 for Band III ($f_{\rm end} = 10^{-2}\,$Hz, $f_{\rm beg} = 10^{3}\,$Hz). This configuration places the stasis feature in the BBO/DECIGO-to-ET frequency range, which has the best projected sensitivity to the IGWB among the considered detectors.

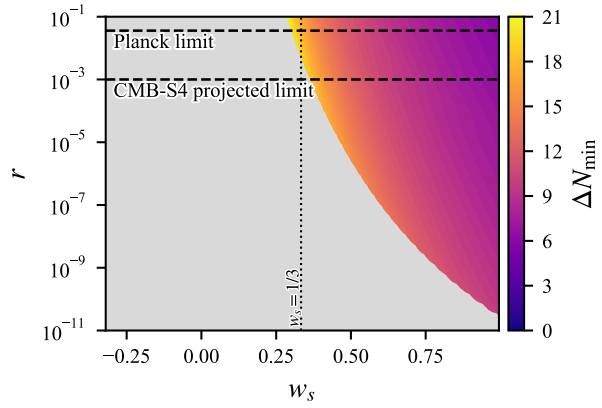
anchors of Table II and lets $f_{\rm beg} = f_{\rm end}\exp[(1+3w_s)\Delta N/2]$ follow from $(w_s, \Delta N)$. We stress that the band labels are used here only as $f_{\rm end}$ anchors, and that unlike the fixed-$(f_{\rm end}, f_{\rm beg})$ configurations of Table II the lever arm $f_{\rm beg}/f_{\rm end}$ varies across each map, growing with both w_s and ΔN. The w_s axis spans $(-1/3, 1)$ continuously, so each map covers the full range of allowed equation of state values. We take the PLS curves of [18] scaled to $T_{\rm obs} = 4\,$yr and $\rho_{\rm thr} = 1$ throughout, and at each grid point evaluate eq. (13) for whichever instrument performs best there.

At the Planck limit $r = 0.036$ the feature remains resolvable down to almost $w_s = 0.1$ in Band III, and down to $w_s \approx 0.6$ at the CMB-S4 projected limit. The gray region marks parameter space in which the feature is undetectable for any ΔN.

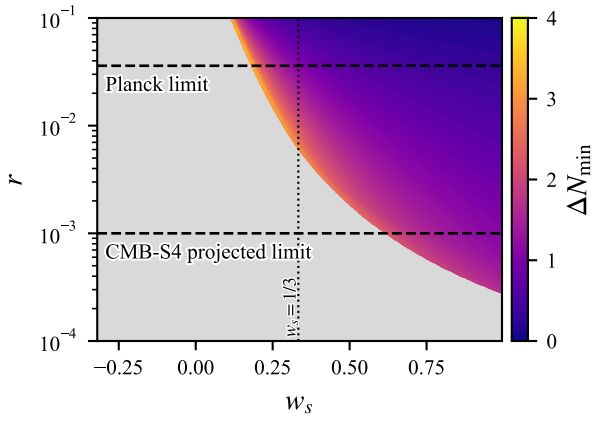
Note. Three caveats should be kept in mind for these plots. First, PLS curves are constructed for pure power-law backgrounds [18], so a broken power law that crosses one attains SNR $\sim \rho_{\rm thr}$



(a) Band I, $f_{\rm end} = 10^{-4}\,$Hz.



(b) Band II, $f_{\rm end} = 10^{-9}\,$Hz.



(c) Band III, $f_{\rm end} = 10^{-2}\,$Hz.

FIG. 4: Shortest detectable stasis duration $\Delta N_{\rm min}$, in e-folds, as a function of the stasis equation of state w_s and the tensor-to-scalar ratio r, for the three band anchors of Table II. At each point the color gives eq. (13) evaluated for the most sensitive instrument, using the PLS curves of [18] with $T_{\rm obs} = 4\,$yr and $\rho_{\rm thr} = 1$. The detection criterion requires both the tilted stasis band and at least one adjacent plateau to cross that instrument's PLS curve, so that α and $\mathcal{C}^2$ are separately measurable and the consistency relation of eq. (7) can be tested. Dashed lines: the Planck/BICEP-Keck upper limit $r < 0.036$ [15] and the CMB-S4 projected limit $r < 10^{-3}$ at 95% CL [28]. Grey: no stasis epoch within the plotted range of ΔN renders the feature detectable. Note that $f_{\rm beg}$ is not fixed but follows from $(w_s, \Delta N)$, so the band labels denote the $f_{\rm end}$ anchor only; the ΔN ranges, and hence the color scales, differ between panels. The vertical dotted line marks $w_s = 1/3$.

only approximately; the maps are accurate at the level of the shape of the detectable region, not the precise placement of its boundary. Second, resolving a deviation from a baseline formally calls for a model-comparison or Fisher analysis rather than an SNR threshold, and the criterion adopted here is the standard SNR-level proxy for it; a full Fisher treatment is deferred to future work (Sec. VI). Third, the maps show the envelope over instruments and therefore identify where a detection is possible, but not by which instrument; the per-detector thresholds quoted in Secs. IV C 1 and IV C 2 and Appendices A and B are obtained from the same calculation applied to each PLS curve separately.

C. Microphysical Realizations of Stasis

In this subsection we discuss the detectability of two specific realizations of stasis, canonical stasis in which the IGWB gets suppressed, and dynamical scalar stasis in which the IGWB gets enhanced. Discussion of the detectability of vacuum-energy/matter stasis and vacuum-energy/radiation stasis can be found in Appendices A and B.

1. *Canonical stasis* ($0 \leq w_s < 1/3$)

Canonical stasis [2] spans $w_s \in [0, 1/3)$, giving $\alpha \in (-2, 0)$: the stasis band is suppressed relative to the RD baseline (a notch), with suppression deepening as $w_s \to 0$ (matter domination). The Bessel amplitude satisfies $\mathcal{C}^2 \in (9/16, 1)$, so the spectrum steps down by at most $\sim 44\%$ at $f_{\rm end}$. The pre-stasis plateau is additionally suppressed by the accumulated tilt factor $(f_{\rm beg}/f_{\rm end})^{\alpha}$, which can be orders of magnitude below the RD baseline for long stasis durations.

Using power-law integrated sensitivity curves [18] scaled to $T_{\rm obs} = 4\,{\rm yr}$ and $\rho_{\rm thr} = 1$, BBO's minimum sensitivity is $h^2\Omega_{\rm GW}^{\rm BBO} \approx 4 \times 10^{-18}$, just below the RD baseline of 6.8×10^{-18} at $r = 0.01$. However, the stasis feature is a *suppression* of the IGWB, so detecting it requires resolving the deviation below the baseline rather than the baseline itself. The suppression deepens as $w_s \to 0$, so the required tensor-to-scalar ratio grows monotonically with decreasing w_s. In Band III, the feature is detectable by BBO for $r \gtrsim 0.01$ at $w_s \approx 0.3$, rising to $r \gtrsim 0.036$ at $w_s \approx 0.2$. DECIGO achieves a minimum sensitivity of $\approx 1.2 \times 10^{-17}$ (4 yr), requiring $r \gtrsim 0.02$ for the flat baseline and somewhat more for the suppressed stasis band.

For Band I (LISA), neither the stasis band nor the RD baseline is reachable at $r = 0.01$:

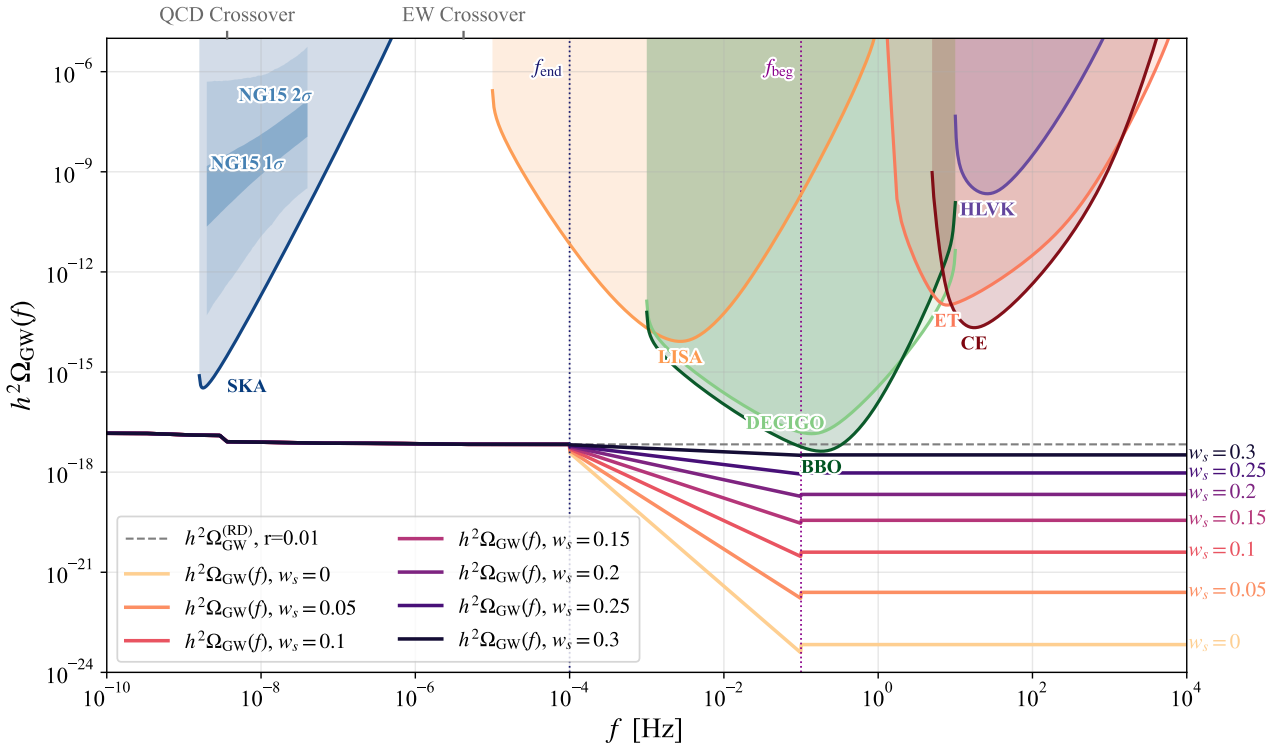


FIG. 5: Stochastic GW background $h^2\Omega_{\rm GW}(f)$ for canonical stasis ($w_s \in [0, 1/3]$) in Band I ($f_{\rm end} = 10^{-4}\,$Hz, $f_{\rm beg} = 10^{-1}\,$Hz; $T_{\rm end} \approx 3.8\,$TeV). Grey dashed: RD baseline at $r = 0.01$. Shaded: detector PLS curves [18] with $T_{obs} = 4$ years and $\rho_{thr} = 1$. Blue band: NANOGrav 15-year posterior [27]. The feature falls in the LISA band; LISA's minimum sensitivity $\sim 810^{-}15$ requires $r \gtrsim 10^3$ for detection, four orders of magnitude above current Planck/BICEP/Keck bounds.

LISA's minimum sensitivity $\sim 810^{-15}$ lies three orders of magnitude above the IGWB for this value of r. LISA becomes competitive only for $r \gtrsim 10$, more than two orders of magnitude above current CMB bounds.

2. *Dynamical scalar stasis* ($1/3 < w_s < 1$)

Dynamical scalar stasis [5] arises when a scalar field sustains a fixed equation of state $w_s \in (1/3, 1)$ through a potential-dominated attractor. The key distinction from the canonical and vacuum-energy scenarios is the sign of the spectral tilt: $\alpha(w_s) > 0$ for $w_s > 1/3$, so the stasis band is *enhanced* relative to the radiation-dominated baseline rather than suppressed. The IGWB rises through the stasis band from $f_{\rm end}$ to $f_{\rm beg}$, reaching a pre-stasis plateau elevated

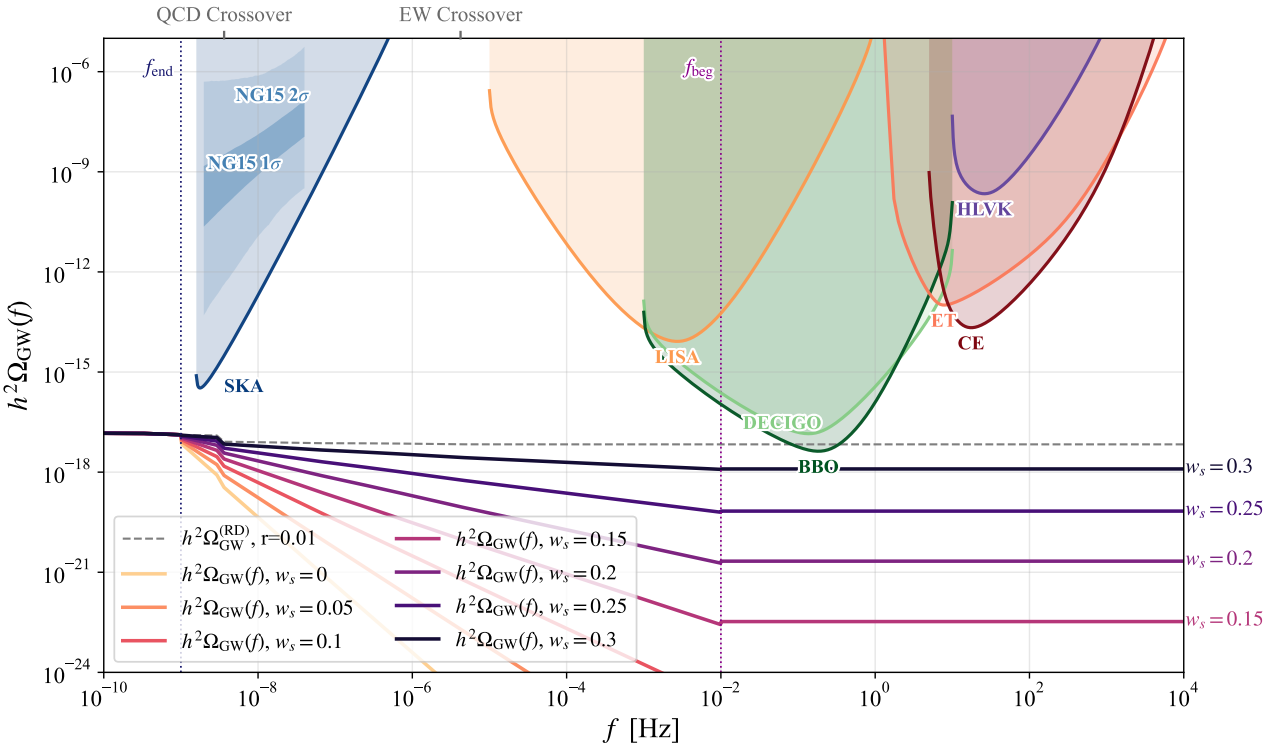


FIG. 6: Same as Fig. 5 for Band II ($f_{\rm end} = 10^{-9}\,$Hz, $f_{\rm beg} = 10^{-2}\,$Hz; $T_{\rm end} \approx 55\,$MeV). The stasis band spans the NANOGrav-to-LISA range; the QCD and EW g_* transitions at 3.6×10^{-9} and $2.6 \times 10^{-6}\,$Hz fall inside the stasis band (see Sec. III). The end-of-stasis temperature is below the QCD crossover and near the BBN epoch, which imposes additional cosmological constraints on this scenario.

above the baseline by the accumulated-tilt factor $(f_{\rm beg}/f_{\rm end})^{\alpha}$. For Band III with $f_{\rm beg}/f_{\rm end} \sim 10^5$ and $w_s \gtrsim 0.5$, this factor reaches 10^2–10^4, and for w_s approaching the kination limit ($w_s \to 1$, $\alpha \to 1$) it can exceed 10^5. For Band II, the plateau can be enhanced by as much as $\sim 10^7$. The crucial observational consequence is a decoupling from r: even if r is far below the projected sensitivity of any CMB experiment, the stasis-enhanced plateau can still be visible to BBO and DECIGO. For Band II, LISA and CE are competitive when r is of $O(0.01)$ for $w_s \gtrsim 0.55$ and ET is competitive when r is of $O(0.01)$ for $w_s \gtrsim 0.65$. For all bands, BBO can detect the stasis feature across the entire $w_s \in (1/3, 1)$ parameter space at $r = 0.01$. As shown in Fig.11, in Band II $r_{\rm min}$ drops below 10^{-7} for $w_s \gtrsim 0.8$. For w_s close to the kination limit, BBO can detect the feature for r as small as $\sim 10^{-9}$, well below the reach of CMB-S4 or LiteBIRD. Figures 8–10 show these spectra for the three frequency bands.

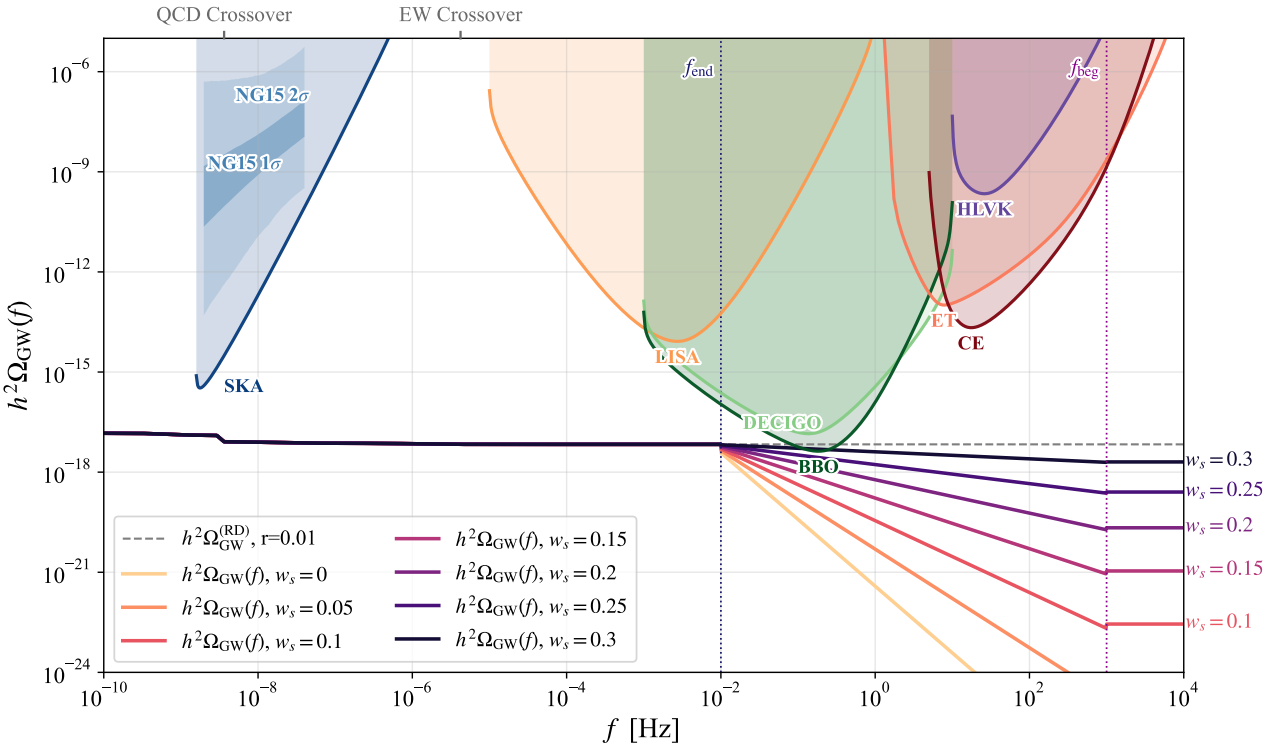


FIG. 7: Same as Fig. 5 for Band III ($f_{\rm end} = 10^{-2}\,$Hz, $f_{\rm beg} = 10^{3}\,$Hz; $T_{\rm end} \approx 380\,$TeV). The stasis band falls squarely in the BBO/DECIGO-to-ET range. For $r \gtrsim$ few $\times\, 0.01$ BBO can detect the stasis feature for large values of w_s within the allowed range for canonical stasis.

In Bands I and II, both the spectral distortion, α, and the amplitude step, $\mathcal{C}^2$, are detectable for almost the full range of w_s values. In Band III, however, only the enhancement is measurable, not the amplitude step. While in Bands I and II the consistency relation (Eq. 7) can be used to verify the occurrence of a stasis epoch or one of its mimics, detection of the enhancement in Band III would at best be a hint of a stasis epoch.

D. Consistency with the $\Delta N_{\rm eff}$ bound

For the enhancement scenarios ($w_s > 1/3$), the pre-stasis plateau rises above the radiation-dominated baseline by the accumulated-tilt factor $(f_{\rm beg}/f_{\rm end})^{\alpha}$, which can reach 10^5–10^7 for the longest-duration configurations. Because a gravitational-wave background contributes to the total radiation energy density, the integrated IGWB is bounded by the same big-bang-nucleosynthesis and CMB constraints on extra relativistic species that limit any dark-radiation

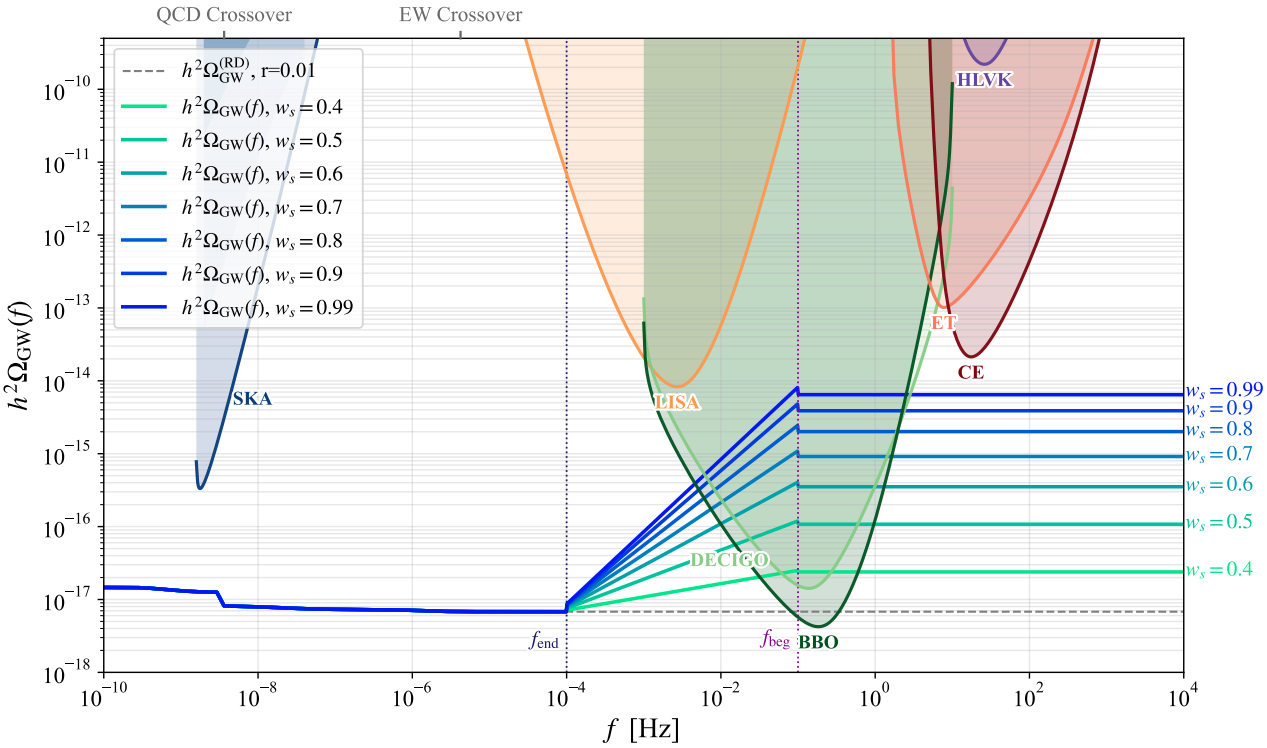


FIG. 8: Stochastic GW background $h^2\Omega_{\rm GW}(f)$ for dynamical scalar stasis ($w_s \in [1/3, 1]$) in Band I ($f_{\rm end} = 10^{-4}\,$Hz, $f_{\rm beg} = 10^{-1}\,$Hz; $T_{\rm end} \approx 3.8\,$TeV). Grey dashed: RD baseline at $r = 0.01$. Shaded: detector PLS curves [18] with $T_{obs} = 4$ years and $\rho_{thr} = 1$. Blue band: NANOGrav 15-year posterior [27]. The feature falls in the LISA band; $\sim 8 \times 10^{-15}$ requires $r \gtrsim 0.1$ for detection, above current Planck/BICEP/Keck bound of 0.036.

component [29, 30],

$$\int h^2\Omega_{\rm GW}(f)\, d\ln f \;\lesssim\; 5.6\times10^{-6}\,\Delta N_{\rm eff}, \tag{14}$$

where the integral runs over all modes that re-entered the horizon before the epoch at which the bound is applied. Taking the conservative post-Planck value $\Delta N_{\rm eff} \lesssim 0.2$ gives a ceiling of $\approx 1.1 \times 10^{-6}$.

The integral is dominated by the high-frequency plateau, where $h^2\Omega_{\rm GW}$ is largest. For enhancement scenarios in which $\alpha > 0$ the plateau height is

$$h^2\Omega_{\rm GW}^{\rm plateau} = \mathcal{C}^2(\nu)\left(\frac{f_{\rm beg}}{f_{\rm end}}\right)^{\alpha} h^2\Omega_{\rm GW}^{\rm (RD)}, \tag{15}$$

and, since the integrand climbs monotonically through the stasis band and is flat above $f_{\rm beg}$, the integral is set by the plateau amplitude times its logarithmic extent, $\int h^2\Omega_{\rm GW}\, d\ln f \sim h^2\Omega_{\rm GW}^{\rm plateau}\,\Delta\ln f_{\rm plateau}$, with the stasis band itself contributing only an $\mathcal{O}(1/\alpha)$ correction.

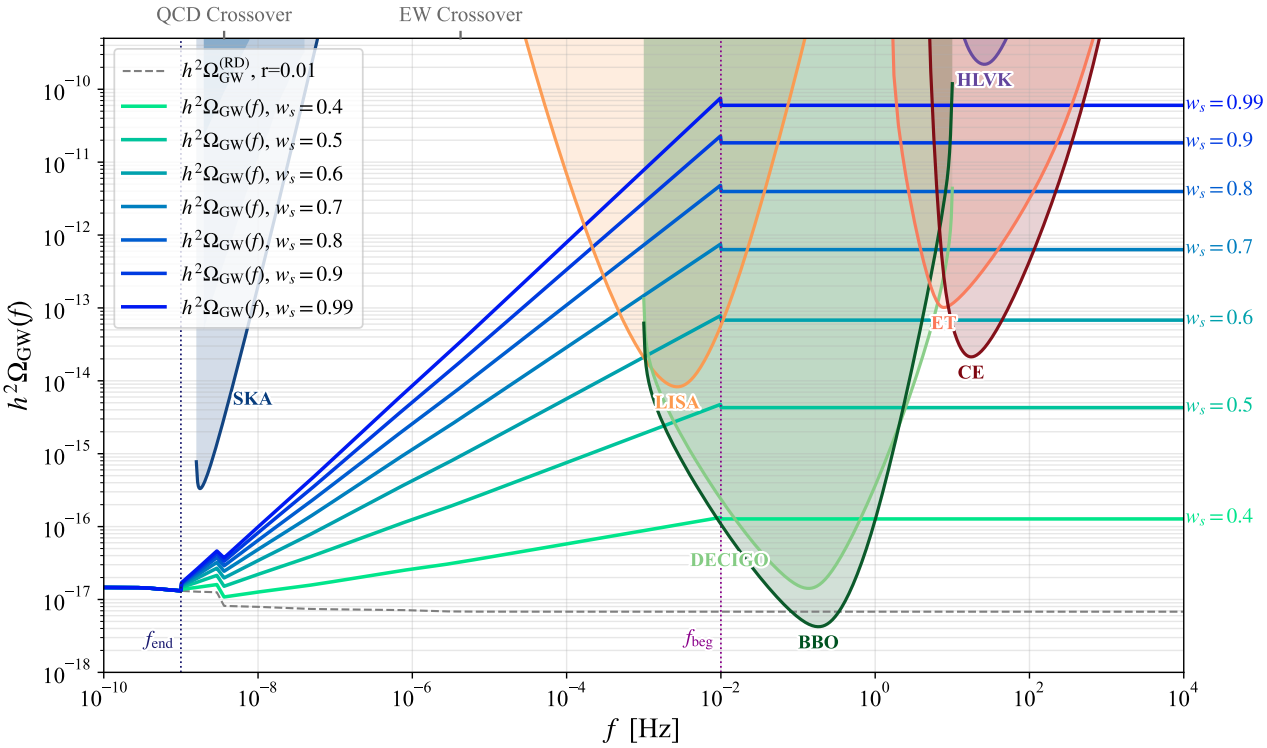


FIG. 9: Same as Fig. 8 for Band II ($f_{\rm end} = 10^{-9}\,$Hz, $f_{\rm beg} = 10^{-2}\,$Hz; $T_{\rm end} \approx 55\,$MeV). The stasis band spans the NANOGrav-to-LISA range; the QCD and EW g_* transitions at 3.6×10^{-9} and $2.6 \times 10^{-6}\,$Hz fall inside the stasis band (see Sec. III). The end-of-stasis temperature is below the QCD crossover and near the BBN epoch, which imposes additional cosmological constraints on this scenario. BBO can detect the stasis feature across the entire dynamical scalar w_s range at $r = 0.01$, with $r_{\rm min}$ falling below 10^{-7} for $w_s \gtrsim 0.8$ (see Sec. IV C 2)

The most stringent case is the one approaching kination ($w_s \to 1$, $\alpha \to 1$, $\mathcal{C}^2 \to 4/\pi$) in Band II, which combines the maximal tilt with the widest lever arm, $f_{\rm beg}/f_{\rm end} = 10^7$. At the Planck upper limit $r = 0.036$ (so $h^2\Omega_{\rm GW}^{\rm (RD)} = 2.4 \times 10^{-17}$), the plateau reaches

$$h^2\Omega_{\rm GW}^{\rm plateau} \approx \frac{4}{\pi} \times 10^7 \times 2.4 \times 10^{-17} \approx 3 \times 10^{-10}. \tag{16}$$

Even allowing the flat plateau to span a further ~ 10 decades in frequency above $f_{\rm beg}$, the integrated energy density is $\int h^2\Omega_{\rm GW}\, d\ln f \sim 10^{-9}$–$10^{-8}$, two to three orders of magnitude below the bound of Eq. (14). All other enhancement configurations have either a smaller tilt, a shorter lever arm, or a lower $f_{\rm end}$-to-$f_{\rm beg}$ ratio, and are correspondingly safer.

The enhancement scenarios therefore remain comfortably consistent with the $\Delta N_{\rm eff}$ bound

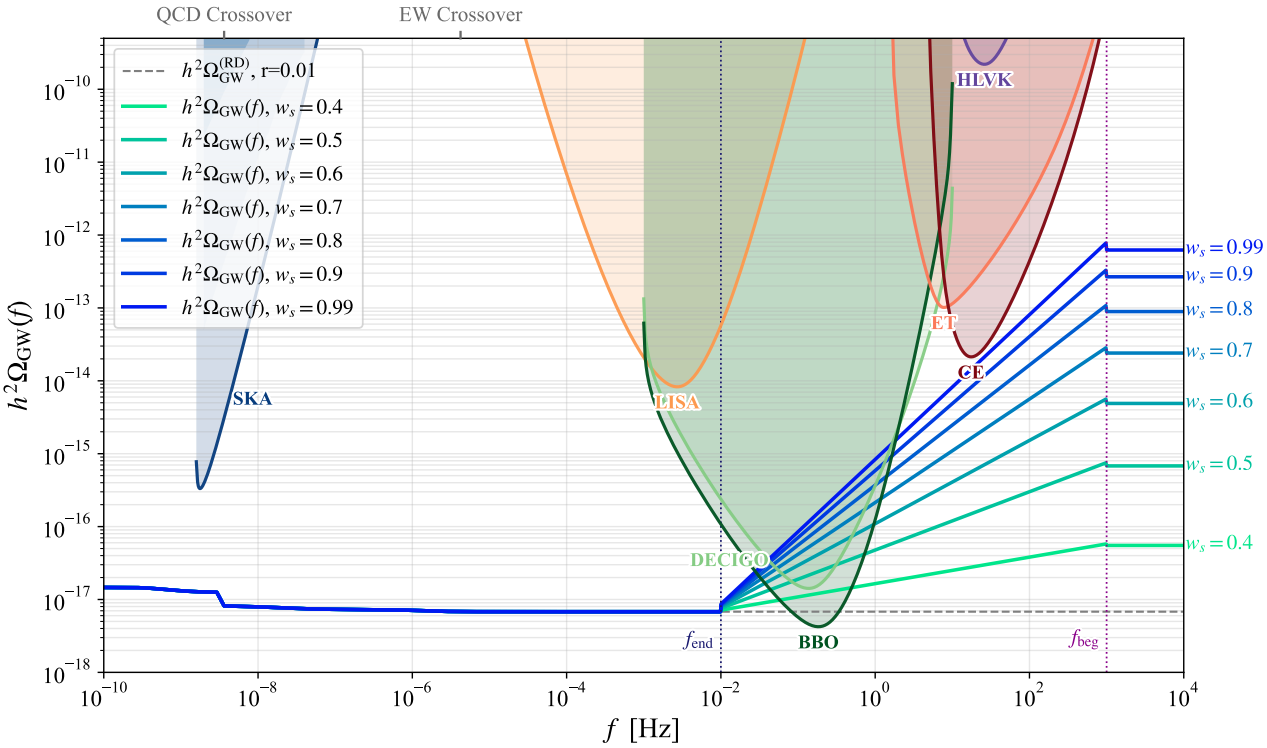


FIG. 10: Same as Fig. 8 for Band III ($f_{\rm end} = 10^{-2}\,$Hz, $f_{\rm beg} = 10^{3}\,$Hz; $T_{\rm end} \approx 380\,$TeV). The stasis band falls squarely in the BBO/DECIGO-to-ET range. BBO can detect the stasis feature across the entire dynamical scalar w_s range at $r = 0.01$.

across the entire $(w_s, \Delta N)$ parameter space considered here, even at the largest tensor-to-scalar ratios allowed by current data. Equivalently, Eq. (14) imposes an upper envelope on the combination $\mathcal{C}^2(f_{\rm beg}/f_{\rm end})^{\alpha}\, r$; saturating it would require either a stasis duration well beyond $\Delta N \sim 40$ e-folds or a tensor amplitude far above the CMB limit, neither of which arises in the scenarios studied here.

E. Which microphysical realizations land where?

The mapping from microphysics to detector band is set by the end-of-stasis temperature $T_{\rm end}$ via eq. (5). Different realizations predict different $T_{\rm end}$ values and therefore probe different frequency bands:

- **Canonical tower / KK:** The decay rate of the last tower species is $\Gamma_{\rm last} \sim H(T_{\rm end})$, with $T_{\rm end}$ set by the lightest species mass. Towers with $m_{\rm min} \sim 1\,$TeV give $T_{\rm end} \sim$ few TeV

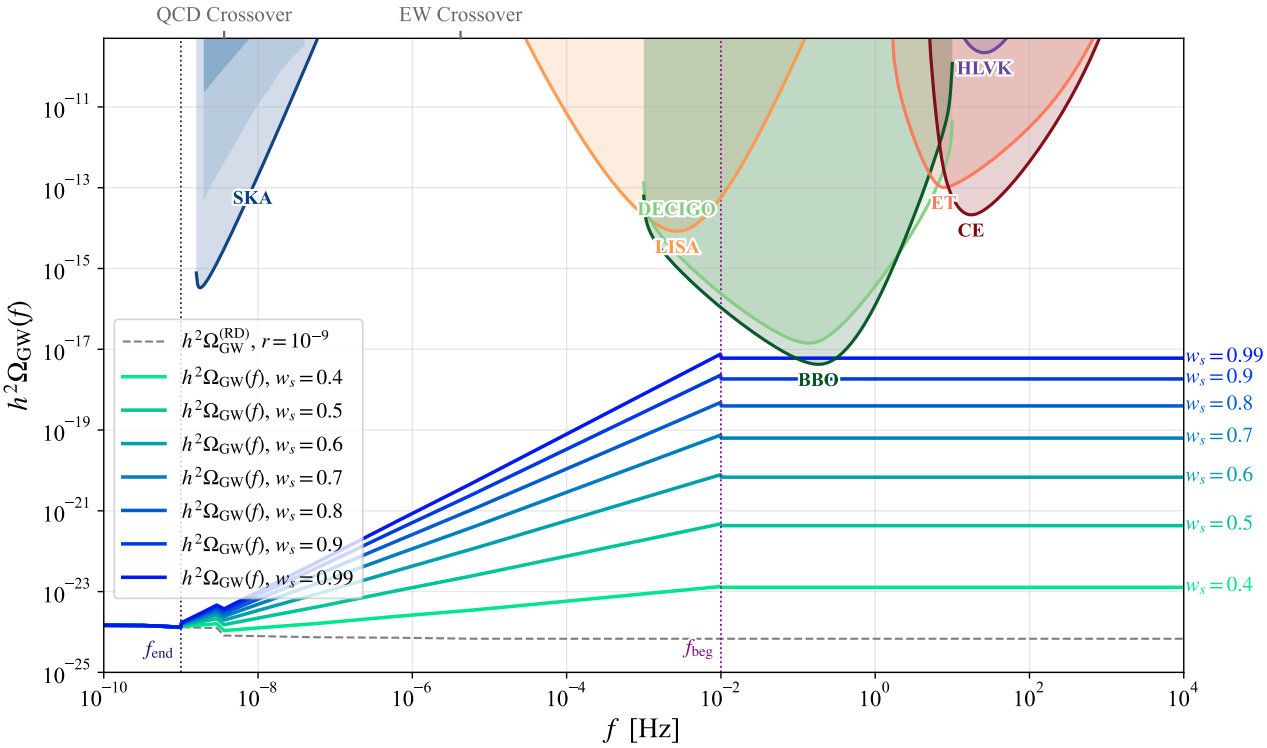


FIG. 11: Stochastic GW background $h^2\Omega_{\rm GW}(f)$ for dynamical scalar stasis ($w_s \in [1/3, 1]$) in Band II with r set to the approximate minimum value for which the spectrum is still detectable by BBO for values of w_s approaching the kination limit, 10^{-9}; $T_{\rm end} \approx 55\,\text{MeV}$. Grey dashed: RD baseline at $r = 10^{-9}$. Shaded: detector PLS curves [18] with $T_{obs} = 4$ years and $\rho_{thr} = 1$. Blue band: NANOGrav 15-year posterior [27].

and $f_{\rm end} \sim 10^{-4}$–$10^{-3}\,\text{Hz}$ (LISA band); lighter towers can push $T_{\rm end}$ down into the DECIGO/BBO band or below.

- **PBH-induced:** The end-of-stasis temperature is set by the evaporation of the heaviest PBHs, with an evaporation temperature, $T_{\rm evap} \propto M_{\rm PBH}^{-3/2}$ [3]. Light PBHs ($M \sim 10^4\,\text{g}$) evaporate at $T \sim 10^4\,\text{GeV}$, placing $f_{\rm end}$ in the LISA band, while heavier PBHs move it down toward the PTA band.

- **Dynamical scalars:** The attractor exit temperature is set by the scalar potential; models explored in [5] span a wide $T_{\rm end}$ range.

- **Thermal annihilation / field-dependent decay:** Both are sensitive to the specific coupling and field-dynamics parameters, making the frequency-band prediction realization-

specific.

The detectability analyses of Sec. IV C 1 and Appendices B and A show that BBO/DECIGO Band III is the most promising configuration for suppression scenarios. This places a rough requirement $T_{\rm end} \sim 10^5$–$4 \times 10^7\,\mathrm{GeV}$ on the preferred realization. Canonical towers and some PBH scenarios satisfy this naturally; the field-dependent and gravitational-interaction realizations would need to be tuned to this range. For scenarios in which the spectrum is enhanced, the stasis feature may be detected in any of the three bands, but is most distinguishable from other models in Bands I and II as both α and $\mathcal{C}^2$ can be detected.

V. END-OF-STASIS TRANSITION: A PHENOMENOLOGICAL TREATMENT

The piecewise spectral template treats the transition out of stasis as instantaneous: w_s jumps discontinuously to 1/3 at $a_{\rm end}$, producing a sharp break in the spectrum at $f_{\rm end}$, which is an approximation and physically imprecise. The attractor that maintains constant Ω_r requires a continuous source of injected energy, and that source must shut off over some finite window: the longest-lived species in a decaying tower has a finite decay time, the lightest PBHs in a mass spectrum evaporate over a tail, the dynamical scalar transitions out of the slow-roll-like regime over a finite range of ϕ, and so on. The result is a smooth transition in $w(t)$ between w_s and 1/3 over some number of e-folds, and a corresponding smoothing of the spectral break.

The same picture applies to the vacuum-energy/matter and vacuum-energy/radiation stases of [31]: the attractor is sustained by a tower of vacuum-like species with equation of state w, and the epoch ends when the longest-lived member of that tower depletes. The transition width is again set by the lifetime of this last component relative to H^{-1} at $a_{\rm end}$, giving $\Delta N_{\rm trans} = \mathcal{O}(1)$ e-folds. Throughout this section we assume the epoch in question lies inside the validity range $w_s > -1/3$; for accelerating epochs, the inflation-like treatment replaces the smoothed-break picture entirely, since there is no in-epoch horizon-crossing event to smooth.

Computing $w(t)$ exactly through the transition is mechanism-specific and is outside of the scope of this paper. The strategy here is instead phenomenological: characterize the transition by a single width parameter and argue analytically how that width smooths the spectrum.

A. The transition width $\Delta N_{\rm trans}$

We define $\Delta N_{\rm trans}$ as the number of e-folds over which the total equation of state interpolates between w_s (the attractor value) and 1/3 (post-stasis RD) at the end of stasis:

$$\Delta N_{\rm trans} \equiv \ln\left(\frac{a_{\rm trans,end}}{a_{\rm trans,beg}}\right), \tag{17}$$

where $a_{\rm trans,beg}$ and $a_{\rm trans,end}$ bracket the window over which w moves substantially from w_s to its RD value, 1/3.

The onset of stasis at $f_{\rm beg}$ is characterised by an independent width $\Delta N_{\rm trans}^{(\rm onset)}$, which is generically different from $\Delta N_{\rm trans}$ because attractor establishment and dissolution are governed by different physics.

a. Mechanism-dependent expectations.

- **Decaying tower (canonical).** The attractor dissolves over a few decay times of the longest-lived species, giving $\Delta N_{\rm trans} = \mathcal{O}(1)$ e-folds.
- **PBH-induced.** The shape of the lower edge of the PBH mass spectrum determines the transition width: narrow spectra give sharper transitions, broad spectra wider ones.
- **Vacuum-energy stases.** The same $\mathcal{O}(1)$ e-fold expectation as the canonical case, with the precise value set by the vacuum-energy tower structure.
- **Dynamical scalar.** The transition width is controlled by the shape of $V(\phi)$ near the exit: steep potentials give sharp transitions, flat ones gradual ones. No general estimate is possible.

The takeaway is that $\Delta N_{\rm trans} = \mathcal{O}(1)$ e-folds is the natural expectation for all realizations with a clear depletion timescale, while mechanism-specific cases require dedicated analysis.

B. How the transition smooths the spectrum

Modes deep inside the horizon during the transition redshift as $h_k \propto 1/a$ regardless of the background equation of state. Modes whose horizon crossing falls within the transition window are affected by the changing equation of state, and their amplitude is interpolated between the stasis-side value $\mathcal{C}^2(\nu_s)$ and the RD-side value $\mathcal{C}^2(1/2) = 1$.

The relation between e-folds of expansion and log-frequency of horizon-crossing modes is set by $aH \propto a^{-(1+3w)/2}$, so a mode crossing ΔN e-folds later sits at log-frequency

$$\Delta \ln f = \frac{1+3w}{2}\,\Delta N \tag{18}$$

relative to the earlier-crossing mode. The total log-frequency range of modes crossing during the transition is therefore

$$\Delta \ln f_{\rm smooth} = \int_{N_{\rm trans,beg}}^{N_{\rm trans,end}} \frac{1+3w(N)}{2}\,dN, \tag{19}$$

which is bounded between

$$\frac{1+3w_s}{2}\,\Delta N_{\rm trans} \;\le\; \Delta \ln f_{\rm smooth} \;\le\; \Delta N_{\rm trans}. \tag{20}$$

For any monotonic profile $w(N)$ that is symmetric about its midpoint (linear, tanh, cubic smoothstep, and most other natural choices), the integral has the closed form

$$\Delta \ln f^{\rm (sym)}_{\rm smooth} = \frac{3(1+w_s)}{4}\,\Delta N_{\rm trans} = \frac{1+3\bar{w}}{2}\,\Delta N_{\rm trans}, \qquad \bar{w} \equiv \frac{w_s+1/3}{2}, \tag{21}$$

as the integral depends only on the average of w over the transition, equal to $\bar{w}$ for any symmetric profile. The result sits at the *arithmetic* midpoint of the bounds in eq. (20) and serves as a representative value for the $\mathcal{O}(1)$ prefactor. Note that eq. (20) is written for the suppression regime $w_s < 1/3$, in which $(1+3w_s)/2 < 1$; for enhancement scenarios with $w_s > 1/3$ the prefactor exceeds unity and the two bounds exchange roles, so that $\Delta N_{\rm trans}$ becomes the lower bound and $(1+3w_s)\Delta N_{\rm trans}/2$ the upper.

Note. Eq. (19) is the transition analogue of the stasis-band width equation. The latter is a special case in which $w(N) = w_s$ is constant, giving $\Delta \ln f = (1+3w_s)/2 \cdot \Delta N$. The transition integrates the same kinematic relation over a window in which w is varying. No new physics is needed.

Deep sub-horizon modes are unaffected

The tensor mode equation $\mu_k'' + (k^2 - a''/a)\mu_k = 0$ in the WKB limit $k^2 \gg a''/a$ gives $\mu_k \approx C\cos(k\tau+\phi)/\sqrt{k}$, a pure oscillation whose amplitude C is frozen at horizon crossing and conserved thereafter, independent of the subsequent background dynamics. Any mode that

crossed the horizon before the transition has its amplitude locked in by the stasis-era Bessel matching; the transition merely rescales it by $1/a$. These modes contribute to the pre-stasis plateau with the standard accumulated tilt $(f_{\rm beg}/f_{\rm end})^{\alpha}$, independent of $\Delta N_{\rm trans}$. Modes that have not yet crossed by $a_{\rm trans,end}$ will cross in the post-stasis RD era and pick up $\mathcal{C}^2(1/2) = 1$, with no memory of the transition shape.

Sharp transitions and Bogoliubov oscillations

The smooth interpolation above is valid when the adiabaticity condition $\Delta N_{\rm trans} \gg 1$ holds. When $\Delta N_{\rm trans} \lesssim 1$, the transition is sudden relative to the mode's oscillation period at horizon crossing, and the Bessel matching can produce non-trivial Bogoliubov mixing: small oscillations imprinted on the spectrum near $f_{\rm end}$. Computing their amplitude and frequency requires solving the mode equation through a specific $w(N)$ profile and is left for future work.

C. Consequences for future observation

The smoothing does not break the consistency framework but changes how the observables are extracted. The slope α is robust to the smoothing provided that $\Delta N_{\rm stasis} \gg \Delta N_{\rm trans} + \Delta N_{\rm trans}^{(\rm onset)}$: in this regime the shoulders at $f_{\rm end}$ and $f_{\rm beg}$ affect only a small fraction of the stasis band, leaving a clean log-linear interior for the slope fit. The amplitude step $\mathcal{C}^2$ becomes a plateau-ratio fit rather than a measured jump: it is extracted from the asymptotic ratio between the post-stasis plateau (extrapolated through the shoulder) and the stasis-band power law. The consistency relation $\mathcal{C}^2 = \mathcal{C}^2(\alpha)$ from [1] continues to hold in the smoothed template.

Note. The bandwidth condition $\Delta N_{\rm stasis} \gg \Delta N_{\rm trans} + \Delta N_{\rm trans}^{(\rm onset)}$ is the practical criterion for whether the stasis feature is observationally well-resolved. For canonical $\Delta N_{\rm trans} = \mathcal{O}(1)$, this requires $\Delta N_{\rm stasis} \gtrsim$ a few, satisfied by all scenarios of phenomenological interest.

Figure 12 shows the spectral template at canonical stasis ($w_s = 1/6$, $\alpha = -2/3$) with the lower break smoothed over the predicted width of eq. (21), for $\Delta N_{\rm trans} \in \{0, 1, 3, 6\}$, with $f_{\rm end} = 10^{-1}\,$Hz placing the smoothed shoulder in the BBO/DECIGO band.

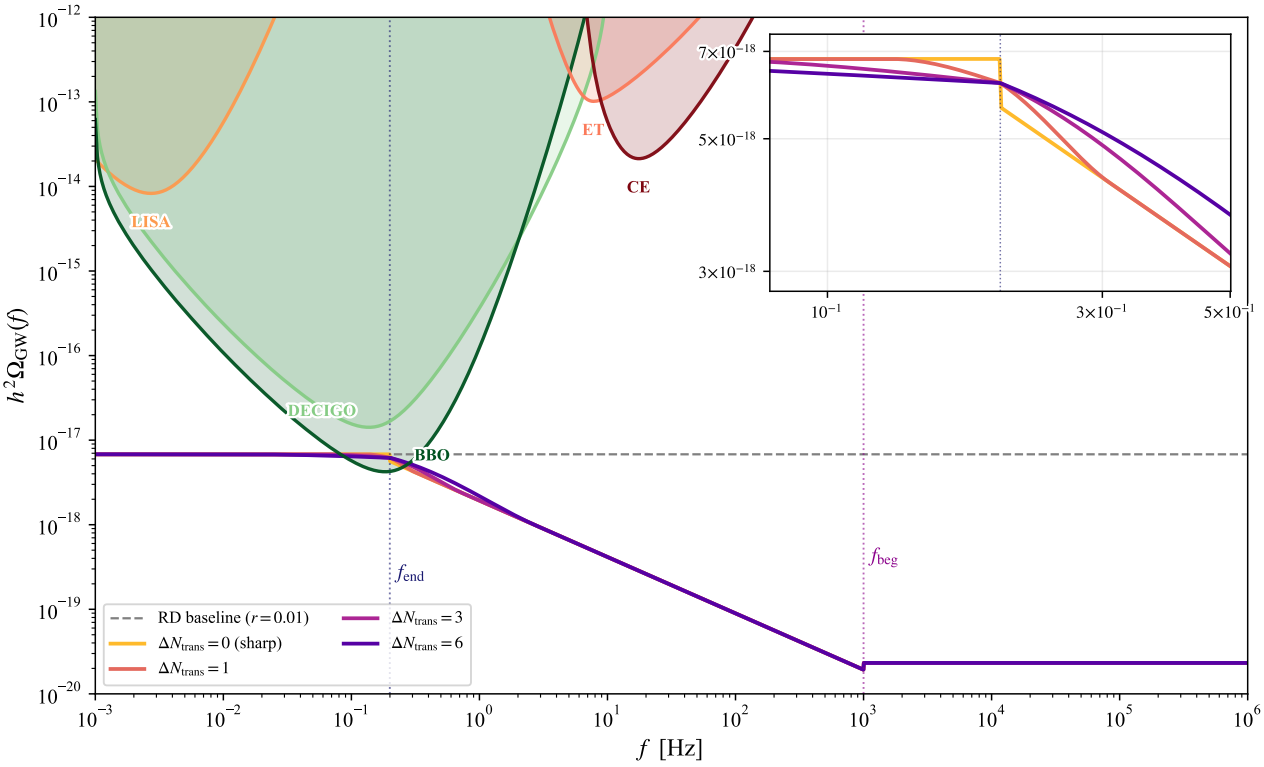


FIG. 12: Spectral template at canonical stasis ($w_s = 1/6$, $\alpha = -2/3$) with the lower break at $f_{\rm end} = 2 \times 10^{-1}$ Hz smoothed over the predicted width of eq. (21), for $\Delta N_{\rm trans} \in \{0, 1, 3, 6\}$. The upper break at $f_{\rm beg}$ is kept sharp. The inset zooms in on the shoulder at $f_{\rm end}$: $\Delta N_{\rm trans} = 1$ produces a small rounding, while $\Delta N_{\rm trans} = 6$ broadens the shoulder over more than a decade. The post-stasis plateau and the stasis-band power law are unaffected away from $f_{\rm end}$. Shaded regions: PLS curves, 4 year observation time [18]; gray dashed: RD baseline at $r = 0.01$.

VI. DISCUSSION AND OUTLOOK

We have presented the full observational prediction for the stasis imprint on the inflationary gravitational wave background, mapped onto the sensitivity landscape of current and future detectors. The main conclusions are:

a. BBO and DECIGO are the primary instruments. Among all planned detectors, BBO and DECIGO offer the most favorable combination of sensitivity and frequency coverage for detecting the stasis feature in the IGWB, with the relative prospects depending strongly on whether the stasis band produces a suppression ($w_s < 1/3$) or an enhancement ($w_s > 1/3$).

For *suppression scenarios* ($w_s < 1/3$), the stasis feature is a notch below the RD baseline.

Using the Schmitz [18] power-law integrated sensitivity curves scaled to $T_{\rm obs} = 4\,\mathrm{yr}$ and $\rho_{\rm thr} = 1$, BBO can detect the stasis feature in Band III for $r \gtrsim 0.01$–0.05 depending on w_s, with deeper notches (smaller w_s) requiring larger r. DECIGO requires $r \gtrsim 0.02$ for a flat spectrum and somewhat more for the suppressed stasis band. LISA, ET, and CE are competitive only for $r \gg 1$, far above current CMB bounds.

For *enhancement scenarios* ($w_s > 1/3$), the pre-stasis plateau rises above the baseline by factors of 10^2–10^5 depending on w_s and the stasis duration. Both BBO and DECIGO can detect the enhancement feature across the entire $(w_s, \Delta N)$ parameter space at $r = 0.01$ for Band III. For w_s approaching the kination limit, BBO can detect the feature at r as small as 10^{-9} for Band II. This decouples the stasis GW signature from the tensor amplitude entirely: a universe with unmeasurably small r can still leave a detectable stasis imprint in the BBO band if the dynamical scalar equation of state is sufficiently large. The combined reach of BBO and DECIGO established in [1] further strengthens this conclusion: jointly, the two instruments can resolve the consistency relation $\mathcal{C}^2 = \mathcal{C}^2(\alpha)$ to $\sigma_\perp \simeq 1.5 \times 10^{-5}$ at $r = 0.01$, providing a sharp test of the stasis hypothesis independent of the underlying microphysical realization.

b. Three independent observables. The stasis GW signature provides three physically distinct observables: (i) the spectral tilt α in the stasis band, which directly encodes w_s; (ii) the amplitude step $\mathcal{C}^2$ at $f_{\rm end}$, which provides the internal consistency check $\mathcal{C}^2 = \mathcal{C}^2(\alpha)$ established in [1]; (iii) the break-shoulder width $\Delta \ln f_{\rm smooth}$, which encodes the transition microphysics through $\Delta N_{\rm trans}$. A detection that simultaneously measures all three quantities would give w_s, $T_{\rm end}$, $\Delta N_{\rm stasis}$, and $\Delta N_{\rm trans}$: a remarkably complete characterization of the stasis epoch.

c. The g_* fine structure as a cross-check. For Band II scenarios ($T_{\rm end} \lesssim T_{\rm QCD}$), the Standard Model g_* transitions at $f_{\rm QCD}$ and $f_{\rm EW}$ produce spectral steps at known, fixed frequencies. These steps must be correctly modeled to extract α and $\mathcal{C}^2$ without bias, but simultaneously provide a non-trivial cross-check: a detection of stasis in Band II should reproduce both the stasis-induced breaks at $f_{\rm end}, f_{\rm beg}$ *and* the SM-predicted steps at $f_{\rm QCD}, f_{\rm EW}$, with the latter at the correct amplitudes. Agreement would constitute strong evidence that the observed spectral feature is genuinely cosmological.

d. Future directions. Several items are deferred to future work. A full Fisher-matrix analysis (parameter estimation precision for w_s, ΔN, $T_{\rm end}$, r) using realistic BBO/DECIGO noise models and including the g_* corrections as fixed nuisance parameters would quantify the measurement reach more precisely than the SNR-based analysis of [1]. The g_* corrections for

Band II also motivate a dedicated study of stasis scenarios with $T_{\rm end}$ near the QCD scale, where the interplay between the stasis spectrum and the hadronic transition could produce richer spectral features. Finally, computing $\Delta N_{\rm trans}$ from first principles for specific realizations, particularly the PBH case [3] and the canonical tower [2], would turn the phenomenological treatment of Sec. V into quantitative predictions.

ACKNOWLEDGMENTS

We would like to thank Tim Tait for the support and valuable feedback on our work. GB is supported by the Spanish grant PID2023-151418NB-I00 funded by MCIU/AEI/10.13039/501100011033. AKB acknowledges support from the "Unit of Excellence Maria de Maeztu 2020-2023" award to the ICC-UB CEX2019-000918-M and grant PID2022-136224NB-C21 funded by MCIN / MINECO / MCOC. AKB and GB are supported by the European Union's Horizon 2020 research and innovation program under the Marie Skłodowska-Curie grant agreement No 860881-HIDDeN, and Horizon Europe research and innovation program under the Marie Skłodowska-Curie Staff Exchange grant agreement No 101086085 – ASYMMETRY.

[1] G. Barenboim and A.-K. Burns, Gravitational Wave Signatures of Cosmological Stasis: A Unified Spectral Template (2026), arXiv:2607.03537 [hep-ph].

[2] K. R. Dienes, L. Heurtier, F. Huang, D. Kim, T. M. Tait, and B. Thomas, Phys. Rev. D **105**, 023530 (2022), arXiv:2111.04753 [astro-ph.CO].

[3] K. R. Dienes, L. Heurtier, F. Huang, D. Kim, T. M. Tait, and B. Thomas, Phys. Rev. D **112**, 083546 (2025), arXiv:2212.01369 [astro-ph.CO].

[4] K. R. Dienes, L. Heurtier, F. Huang, T. M. Tait, and B. Thomas, Phys. Rev. D **112**, 083547 (2025), arXiv:2510.06551 [astro-ph.CO].

[5] K. R. Dienes, L. Heurtier, F. Huang, T. M. Tait, and B. Thomas, Phys. Rev. D **110**, 123514 (2024), arXiv:2406.06830 [astro-ph.CO].

[6] J. Barber, K. R. Dienes, and B. Thomas, Phys. Rev. D **110**, 123515 (2024), arXiv:2408.16255 [astro-ph.CO].

[7] J. Barber, K. R. Dienes, and B. Thomas, Phys. Rev. D **111**, 063519 (2025), arXiv:2412.09123 [astro-ph.CO].

[8] F. Huang and V. Knapp-Pérez, JHEP **09**, 072, arXiv:2502.20449 [hep-ph].

[9] A. J. Long, B. Shams Es Haghi, and M. Venegas, JCAP **01**, 037, arXiv:2506.04502 [hep-ph].

[10] J. Halverson and S. Pandya, Phys. Rev. D **110**, 075041 (2024), arXiv:2408.00835 [hep-ph].

[11] A. A. Starobinsky, JETP Lett. **30**, 682 (1979).

[12] V. A. Rubakov, M. V. Sazhin, and A. V. Veryaskin, Phys. Lett. B **115**, 189 (1982).

[13] L. A. Boyle and P. J. Steinhardt, Phys. Rev. D **77**, 063504 (2008), arXiv:astro-ph/0512014 [astro-ph].

[14] Planck Collaboration, Y. Akrami, F. Arroja, M. Ashdown, J. Aumont, *et al.*, Astron. Astrophys. **641**, A10 (2020), arXiv:1807.06211 [astro-ph.CO].

[15] BICEP/Keck Collaboration, Phys. Rev. Lett. **127**, 151301 (2021), arXiv:2110.00483 [astro-ph.CO].

[16] Y. Watanabe and E. Komatsu, Phys. Rev. D **73**, 123515 (2006), arXiv:astro-ph/0604176.

[17] M. Laine and M. Meyer, JCAP **07**, 035, arXiv:1503.04935 [hep-ph].

[18] K. Schmitz, JHEP **01**, 097, compilation of power-law-integrated sensitivity curves for current and proposed GW detectors; data archived at Zenodo:3689582, arXiv:2002.04615 [hep-ph].

[19] Z. Arzoumanian *et al.* (NANOGrav), Astrophys. J. Lett. **905**, L34 (2020), arXiv:2009.04496 [astro-ph.HE].

[20] S. Chen *et al.* (EPTA), Mon. Not. Roy. Astron. Soc. **508**, 4970 (2021), arXiv:2110.13184 [astro-ph.HE].

[21] G. Janssen, G. Hobbs, M. McLaughlin, C. Bassa, A. Deller, M. Kramer, K. Lee, C. Mingarelli, P. Rosado, S. Sanidas, A. Sesana, L. Shao, I. Stairs, B. Stappers, and J. P. W. Verbiest, PoS **AASKA14**, 037 (2015), arXiv:1501.00127 [astro-ph.IM].

[22] P. Amaro-Seoane *et al.* (LISA), Laser Interferometer Space Antenna (2017), arXiv:1702.00786 [astro-ph.IM].

[23] S. Kawamura *et al.*, Class. Quant. Grav. **28**, 094011 (2011).

[24] V. Corbin and N. J. Cornish, Class. Quant. Grav. **23**, 2435 (2006), arXiv:gr-qc/0512039.

[25] M. Punturo *et al.*, Classical and Quantum Gravity **27**, 194002 (2010).

[26] D. Reitze *et al.*, Bull. Am. Astron. Soc. **51**, 035 (2019), arXiv:1907.04833 [astro-ph.IM].

[27] G. Agazie *et al.* (NANOGrav), Astrophys. J. Lett. **951**, L8 (2023), arXiv:2306.16213 [astro-ph.HE].

[28] K. N. Abazajian *et al.* (CMB-S4), *CMB-S4 Science Book, First Edition* (2016) arXiv:1610.02743 [astro-ph.CO].

[29] M. Maggiore, Phys. Rept. **331**, 283 (2000), arXiv:gr-qc/9909001.

[30] C. Caprini and D. G. Figueroa, Class. Quant. Grav. **35**, 163001 (2018), arXiv:1801.04268 [astro-ph.CO].

[31] K. R. Dienes, L. Heurtier, F. Huang, T. M. Tait, and B. Thomas, Phys. Rev. D **109**, 083508 (2024), arXiv:2309.10345 [astro-ph.CO].

Appendix A: Vacuum-energy/matter stasis ($-1/3 < w_s < 0$)

In the vacuum-energy/matter scenario of [31] (Sec. III therein), the stasis attractor sustains a non-zero vacuum-energy fraction alongside matter, giving an effective equation of state $w_s \in (-1/3, 0)$. The spectral tilt $\alpha < -2$ is more negative than in the canonical case, meaning the stasis band is *more* strongly suppressed than under matter domination. The Bessel amplitude $\mathcal{C}^2 < 9/16$ decreases further below unity as $w_s \to -1/3$, the validity boundary below which the expansion is accelerating and no in-stasis horizon crossing occurs.

This additional suppression has two observational consequences. First, for fixed r the signal in the stasis band is weaker than in the canonical case, making detection harder. Second, the pre-stasis plateau is suppressed by $(f_{\rm beg}/f_{\rm end})^{\alpha}$ with $\alpha < -2$, which for moderate ΔN already brings the plateau to effectively zero, making the multi-epoch comb structure discussed in [1] correspondingly harder to resolve.

Figures 13–15 show the vacuum-energy/matter spectra for the same three frequency bands. Detecting stasis of this type is challenging due to the large suppression of the signal for all allowed values of w_s. This feature could be detectable for allowed values of r in the fine tuned scenario in which $f_{\rm end}$ coincides with the minimum of the BBO PLS curve.

Appendix B: Vacuum-energy/radiation stasis ($-1/3 < w_s < 1/3$)

The vacuum-energy/radiation stasis scenario of [31] (Sec. IV therein) covers $w_s \in (-1/3, 1/3)$, encompassing the canonical and vacuum-energy/matter ranges. The figures below therefore display the union of the spectral shapes seen in the previous two subsections, smoothly interpolating from the more suppressed ($w_s < 0$) to the less suppressed ($w_s > 0$) regimes.

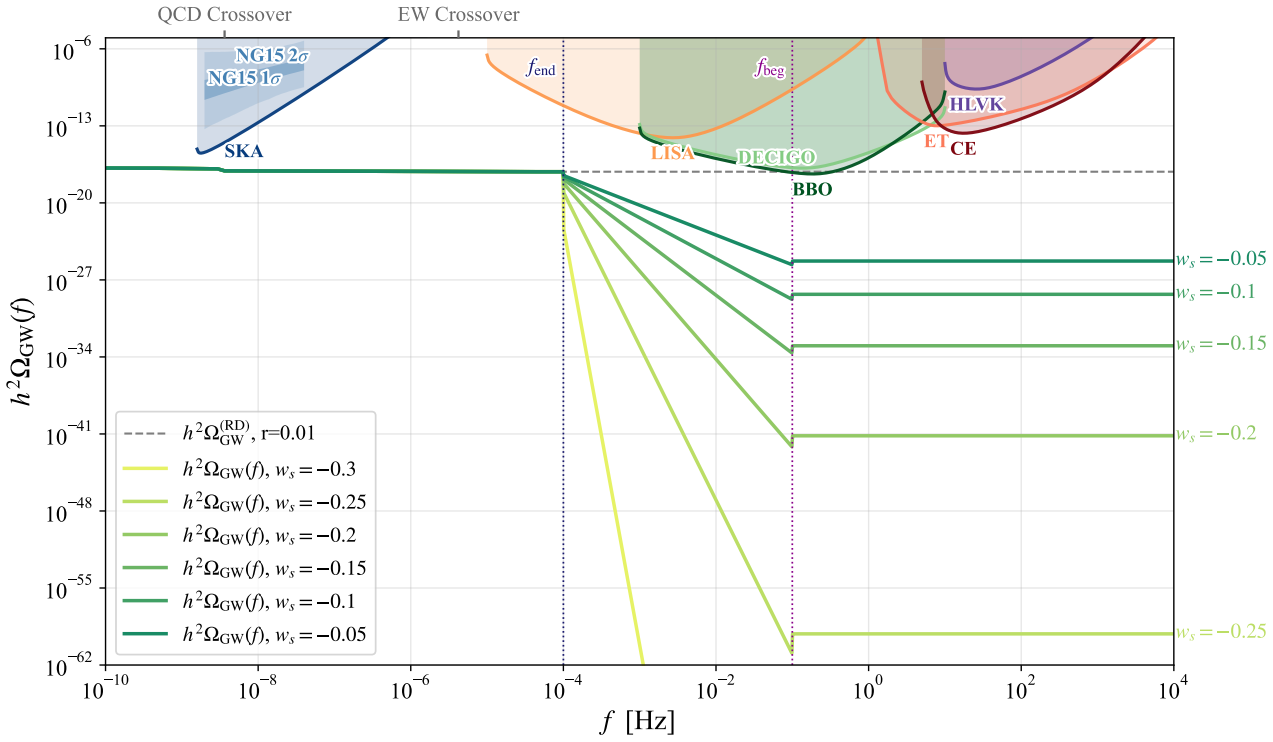


FIG. 13: Stochastic GW background $h^2\Omega_{\rm GW}(f)$ for vacuum-energy/matter stasis ($w_s \in (-1/3, 0)$) in Band I. Grey dashed: RD baseline at $r = 0.01$. Shaded: PLS curves [18]. Blue band: NANOGrav 15-year posterior [27]. The deeper suppression relative to canonical stasis is visible as a more negative slope α in the stasis band.

Figures 16–18 show the spectra. The detectability conclusions mirror those of the canonical and VE/M cases above: Band III placed in the BBO/DECIGO range is the most favorable configuration, with BBO capable of detecting the stasis feature for $r \gtrsim 0.01$ for large values of w_s within the allowed range.

Appendix C: Additional plots: r = 0.036

In this appendix we provide plots of $h^2\Omega_{\rm GW}(f)$ for all four models we cover in this paper for the tensor-to-scalar ratio r set to the upper limit provided by Planck, r = 0.036.

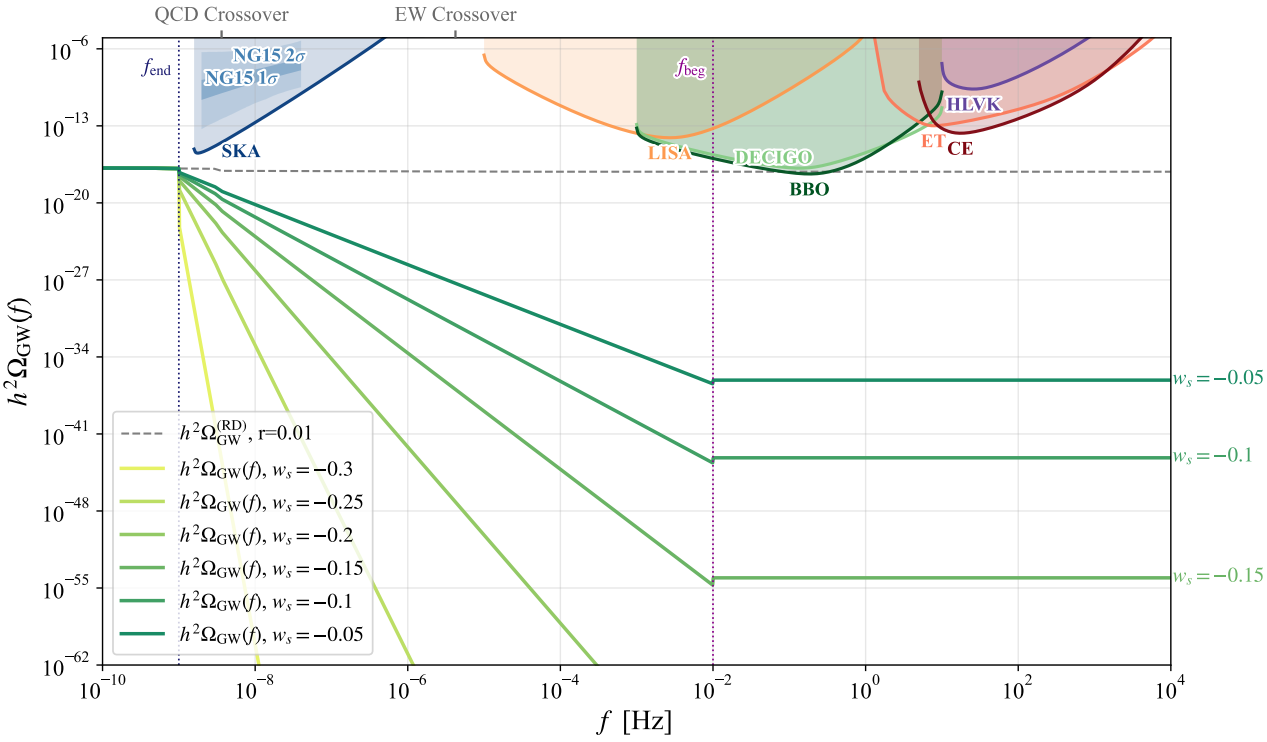


FIG. 14: Same as Fig. 13 for Band II ($T_{\rm end} \approx 55\,{\rm MeV}$). The g_* steps at $f_{\rm QCD}$ and $f_{\rm EW}$ fall within the stasis band for this configuration.

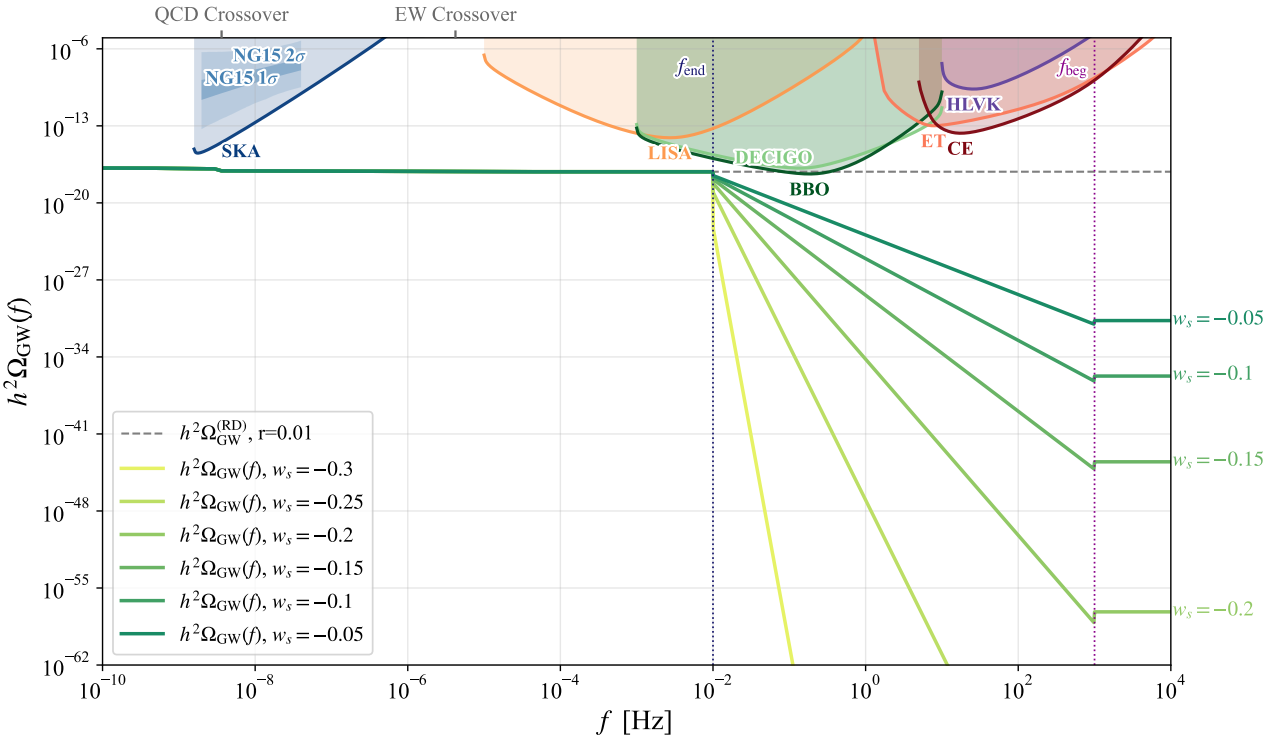


FIG. 15: Same as Fig. 13 for Band III. The steep suppression at high frequencies makes detection progressively harder for $w_s \ll 0$.

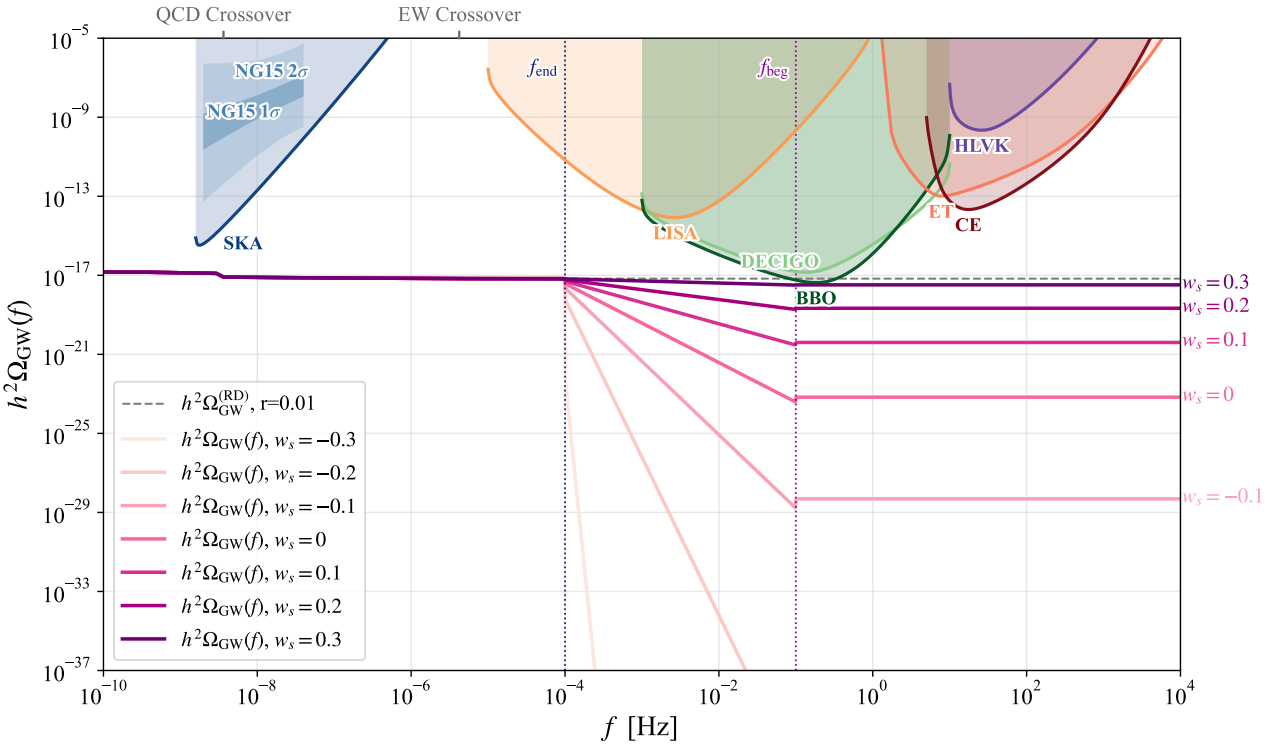


FIG. 16: Stochastic GW background $h^2\Omega_{\rm GW}(f)$ for vacuum-energy/radiation stasis ($w_s \in (-1/3, 1/3)$) in Band I. Grey dashed: RD baseline at $r = 0.01$. Shaded: PLS curves [18]. Blue band: NANOGrav 15-year posterior [27].

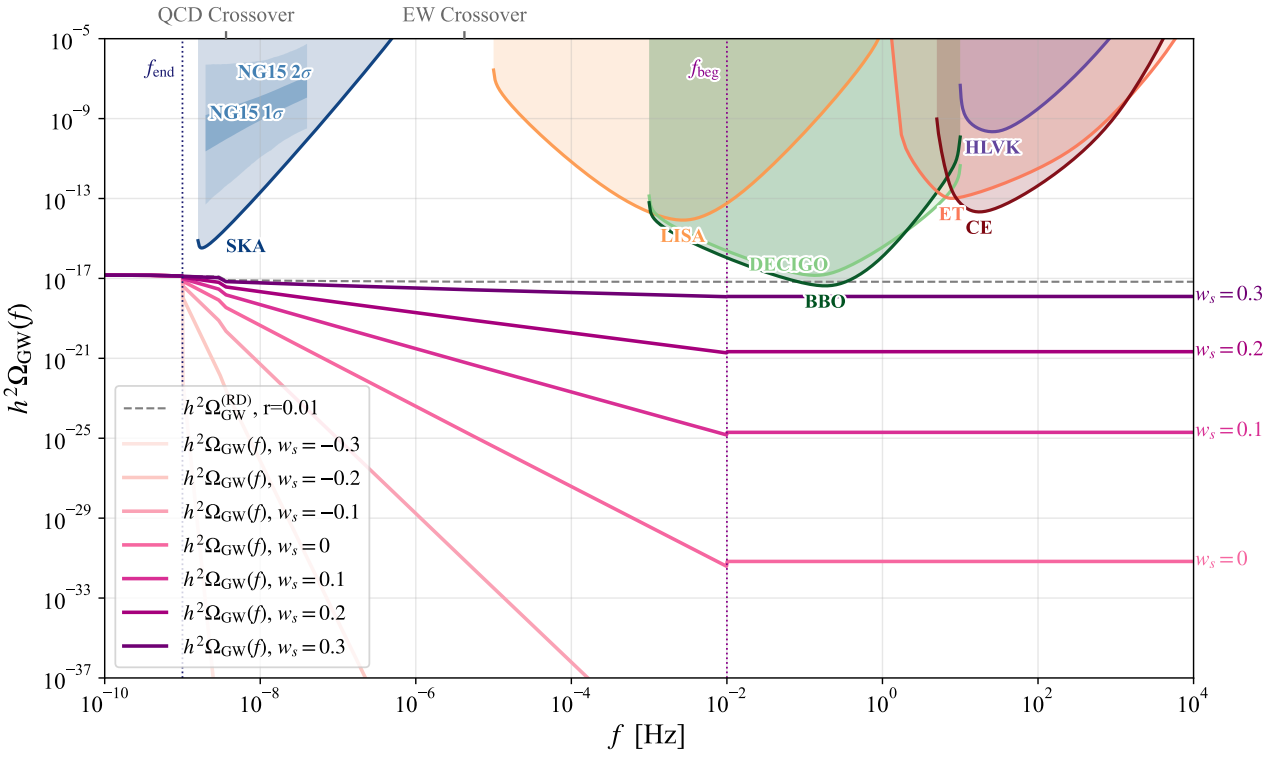


FIG. 17: Same as Fig. 16 for Band II. The g_* steps at $f_{\rm QCD}$ and $f_{\rm EW}$ are present within the stasis band for this configuration.

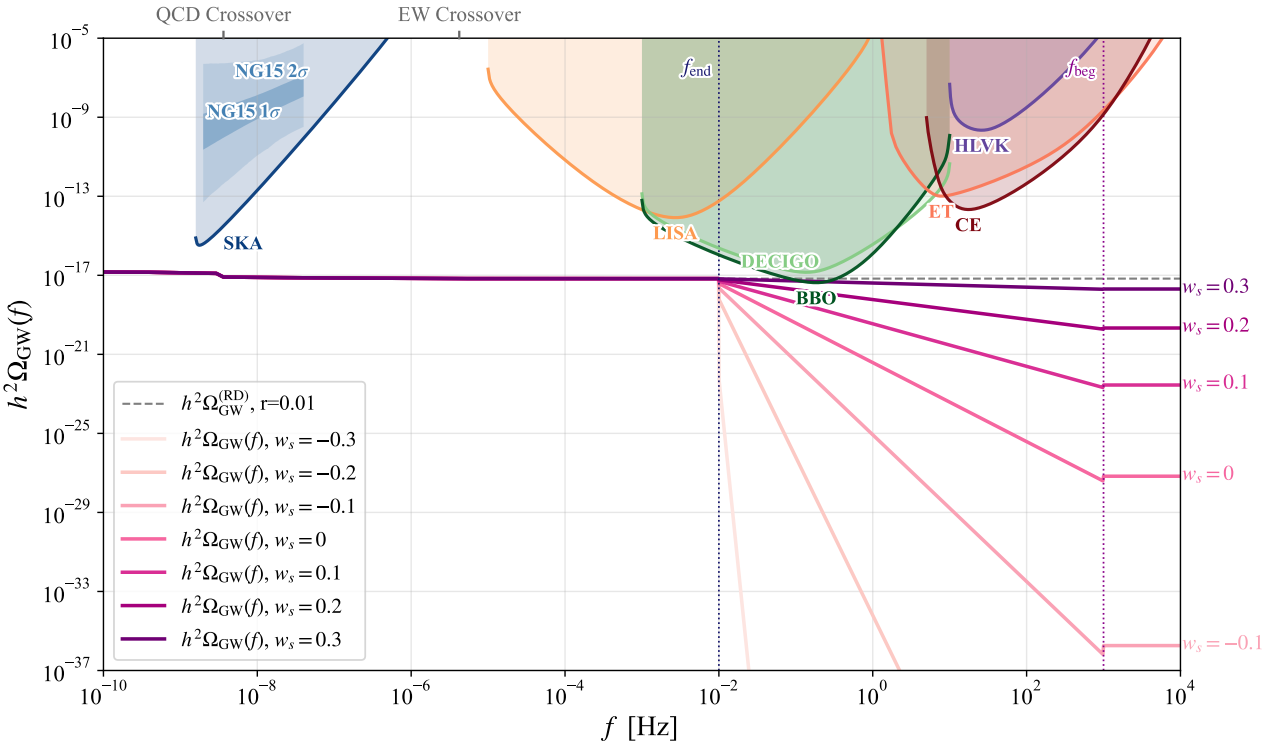
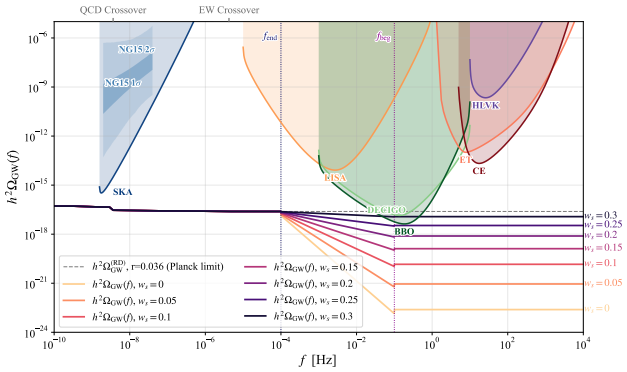
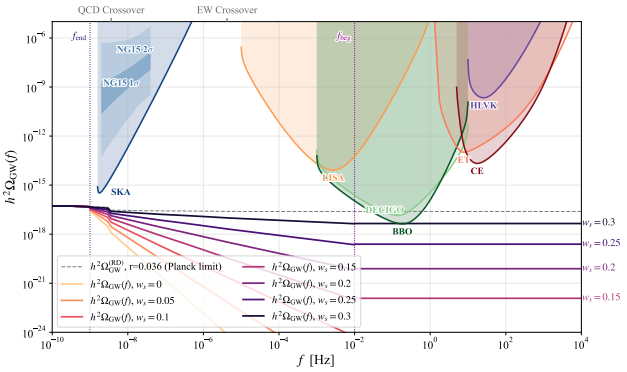


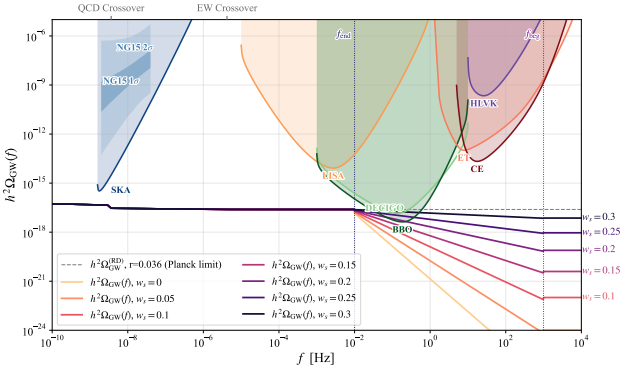
FIG. 18: Same as Fig. 16 for Band III. The spectral template spans the full w_s range, from strong suppression ($w_s \to -1/3$) to the flat RD baseline ($w_s = 1/3$).



(a) Band I, $f_{\rm end} = 10^{-4}\,\mathrm{Hz}$, $f_{\rm beg} = 10^{-1}\,\mathrm{Hz}$; $T_{\rm end} \approx 3.8\,\mathrm{TeV}$.

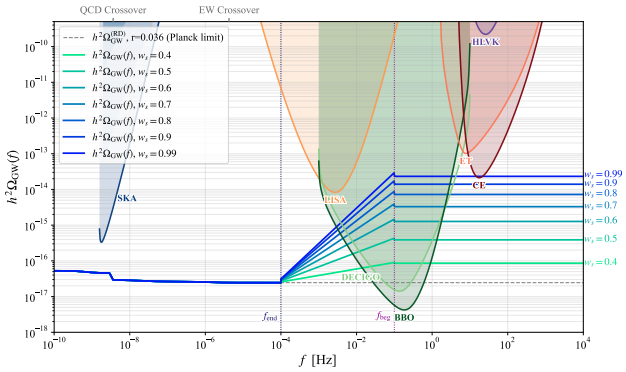


(b) Band II, $f_{\rm end} = 10^{-9}\,\mathrm{Hz}$, $f_{\rm beg} = 10^{-2}\,\mathrm{Hz}$; $T_{\rm end} \approx 55\,\mathrm{MeV}$.

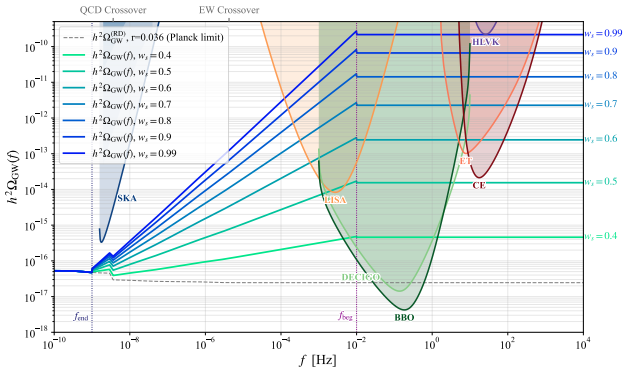


(c) Band III, $f_{\rm end} = 10^{-2}\,\mathrm{Hz}$, $f_{\rm beg} = 10^{3}\,\mathrm{Hz}$; $T_{\rm end} \approx 380\,\mathrm{TeV}$.

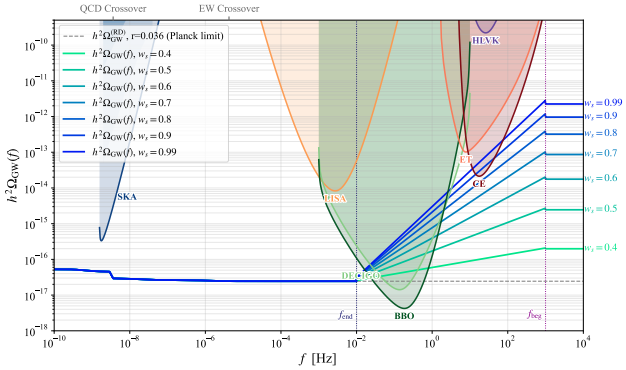
FIG. 19: Stochastic GW background $h^2\Omega_{\rm GW}(f)$ for canonical stasis ($w_s \in [0, 1/3]$) across three frequency bands. Grey dashed: RD at $r = 0.036$ (Planck upper limit). Shaded: detector PLS curves [18] with $T_{obs} = 4$ years and $\rho_{thr} = 1$. Blue band: NANOGrav 15-year posterior [27].



(a) Band I, $f_{\rm end} = 10^{-4}\,\mathrm{Hz}$, $f_{\rm beg} = 10^{-1}\,\mathrm{Hz}$; $T_{\rm end} \approx 3.8\,\mathrm{TeV}$.

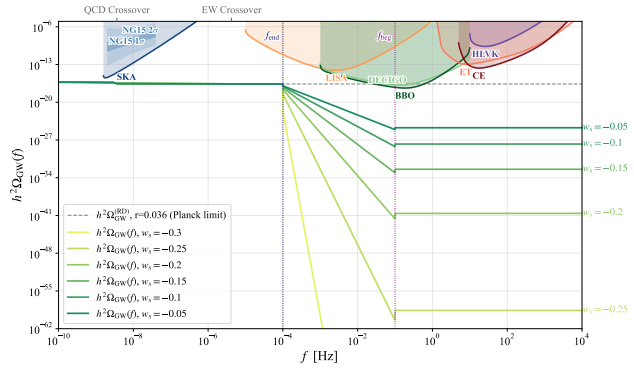


(b) Band II, $f_{\rm end} = 10^{-9}\,\mathrm{Hz}$, $f_{\rm beg} = 10^{-2}\,\mathrm{Hz}$; $T_{\rm end} \approx 55\,\mathrm{MeV}$.

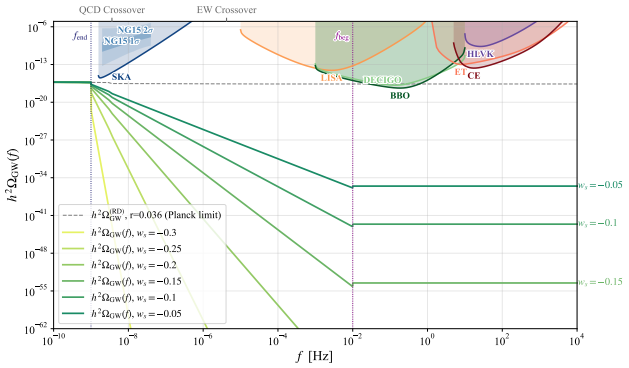


(c) Band III, $f_{\rm end} = 10^{-2}\,\mathrm{Hz}$, $f_{\rm beg} = 10^{3}\,\mathrm{Hz}$; $T_{\rm end} \approx 380\,\mathrm{TeV}$.

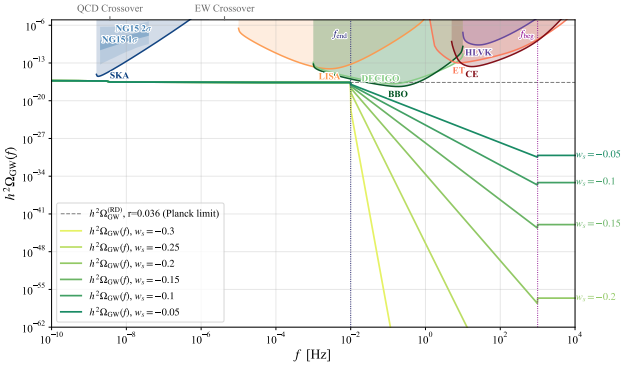
FIG. 20: Stochastic GW background $h^2\Omega_{\rm GW}(f)$ for dynamical scalar stasis ($w_s \in [1/3, 1]$) across three frequency bands. Grey dashed: RD baseline at $r = 0.036$ (Planck upper limit). Shaded: detector PLS curves [18] with $T_{obs} = 4$ years and $\rho_{thr} = 1$. Blue band: NANOGrav 15-year posterior [27].



(a) Band I, $f_{\rm end} = 10^{-4}\,\mathrm{Hz}$, $f_{\rm beg} = 10^{-1}\,\mathrm{Hz}$; $T_{\rm end} \approx 3.8\,\mathrm{TeV}$.

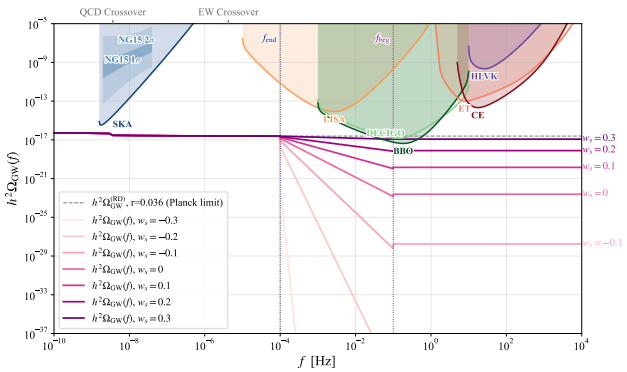


(b) Band II, $f_{\rm end} = 10^{-9}\,\mathrm{Hz}$, $f_{\rm beg} = 10^{-2}\,\mathrm{Hz}$; $T_{\rm end} \approx 55\,\mathrm{MeV}$.

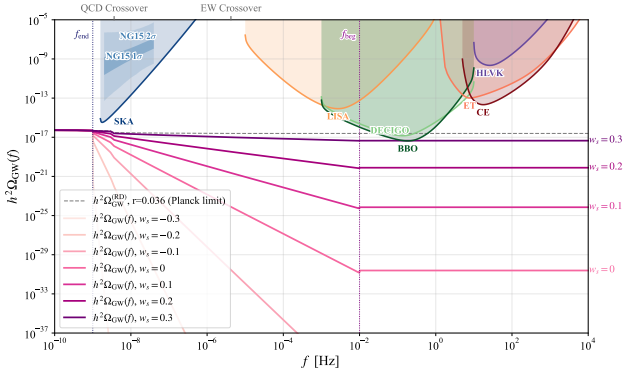


(c) Band III, $f_{\rm end} = 10^{-2}\,\mathrm{Hz}$, $f_{\rm beg} = 10^{3}\,\mathrm{Hz}$; $T_{\rm end} \approx 380\,\mathrm{TeV}$.

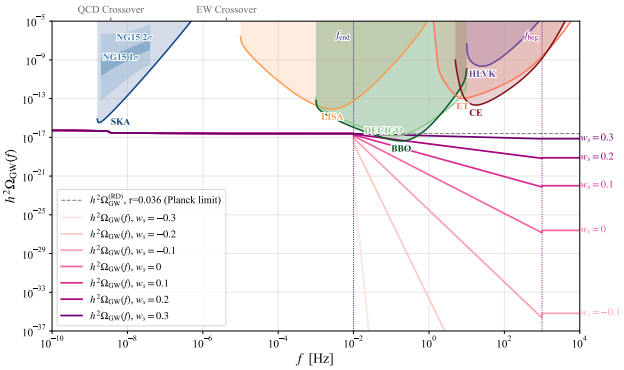
FIG. 21: Stochastic GW background $h^2\Omega_{\rm GW}(f)$ for vacuum-energy/matter stasis ($w_s \in (-1/3, 0)$) across three frequency bands. Grey dashed: RD baseline at $r = 0.036$ (Planck upper limit). Shaded: detector PLS curves [18] with $T_{obs} = 4$ years and $\rho_{thr} = 1$. Blue band: NANOGrav 15-year posterior [27].



(a) Band I, $f_{\rm end} = 10^{-4}\,$Hz, $f_{\rm beg} = 10^{-1}\,$Hz; $T_{\rm end} \approx 3.8\,$TeV.



(b) Band II, $f_{\rm end} = 10^{-9}\,$Hz, $f_{\rm beg} = 10^{-2}\,$Hz; $T_{\rm end} \approx 55\,$MeV.



(c) Band III, $f_{\rm end} = 10^{-2}\,$Hz, $f_{\rm beg} = 10^{3}\,$Hz; $T_{\rm end} \approx 380\,$TeV.

FIG. 22: Stochastic GW background $h^2\Omega_{\rm GW}(f)$ for vacuum-energy/radiation stasis ($w_s \in (-1/3, 1/3)$) across three frequency bands. Grey dashed: RD baseline at $r = 0.036$ (Planck upper limit). Shaded: detector PLS curves [18] with $T_{obs} = 4$ years and $\rho_{thr} = 1$. Blue band: NANOGrav 15-year posterior [27].